



Stability of an isolated pancake vortex in continuously stratified-rotating fluids

Eunok Yim, Paul Billant, Claire Menesguen

► To cite this version:

Eunok Yim, Paul Billant, Claire Menesguen. Stability of an isolated pancake vortex in continuously stratified-rotating fluids. *Journal of Fluid Mechanics*, 2016, 801, pp.508-553. 10.1017/jfm.2016.402 . hal-04201722

HAL Id: hal-04201722

<https://hal.science/hal-04201722>

Submitted on 15 Sep 2023

HAL is a multi-disciplinary open access archive for the deposit and dissemination of scientific research documents, whether they are published or not. The documents may come from teaching and research institutions in France or abroad, or from public or private research centers.

L'archive ouverte pluridisciplinaire **HAL**, est destinée au dépôt et à la diffusion de documents scientifiques de niveau recherche, publiés ou non, émanant des établissements d'enseignement et de recherche français ou étrangers, des laboratoires publics ou privés.

Stability of an isolated pancake vortex in continuously stratified-rotating fluids

Yim Eunok ^{1,*}, Billant Paul ¹, Menesguen Claire ²

¹ Ecole Polytech, CNRS, LadHyX, F-91128 Palaiseau, France.

² CNRS, IFREMER, LPO, BP 70, F-29280 Plouzane, France.

* Corresponding author : Eunok Yim, email address : eunok@ladhyx.polytechnique.fr

Abstract :

This paper investigates the stability of an axisymmetric pancake vortex with Gaussian angular velocity in radial and vertical directions in a continuously stratified-rotating fluid. The different instabilities are determined as a function of the Rossby number Ro , Froude number Fh , Reynolds number Re and aspect ratio α . Centrifugal instability is not significantly different from the case of a columnar vortex due to its short-wavelength nature: it is dominant when the absolute Rossby number $|Ro|$ is large and is stabilized for small and moderate $|Ro|$ when the generalized Rayleigh discriminant is positive everywhere. The Gent–McWilliams instability, also known as internal instability, is then dominant for the azimuthal wavenumber $m=1$ when the Burger number $Bu=\alpha^2 Ro^2/(4F^2h)$ is larger than unity. When $Bu \leq 0.7Ro+0.1$, the Gent–McWilliams instability changes into a mixed baroclinic–Gent–McWilliams instability. Shear instability for $m=2$ exists when Fh/α is below a threshold depending on Ro . This condition is shown to come from confinement effects along the vertical. Shear instability transforms into a mixed baroclinic–shear instability for small Bu . The main energy source for both baroclinic–shear and baroclinic–Gent–McWilliams instabilities is the potential energy of the base flow instead of the kinetic energy for shear and Gent–McWilliams instabilities. The growth rates of these four instabilities depend mostly on Fh/α and Ro . Baroclinic instability develops when $Fh/\alpha|1+1/Ro| \geq 1.46$ in qualitative agreement with the analytical predictions for a bounded vortex with angular velocity slowly varying along the vertical.

Keywords : geophysical and geological flows, vortex flows, vortex instability

1 Introduction

Vortices in geophysical flows have received much attention, especially in the oceans, due to their important role in energy and scalar transports as well as mixing. For example, Meddies (Mediterranean eddies) are formed by warm salty water flowing from the Mediterranean sea into the Atlantic ocean. These mesoscale

vortices can live years traveling in the ocean (Armi *et al.*, 1989; Hobbs, 2007; Ménesguen *et al.*, 2012a). Their thickness is about 1km and their diameter about 100km (Richardson *et al.*, 2000). Similar eddies called Ulleung eddies are formed by warm northward and cold southward currents in East/Japan sea. Once formed, the eddies are trapped in Ulleung basin near Ulleung island (Chang *et al.*, 2004). These eddies are also pancake shaped with both warm and cold core, and a life time around a couple of years. The characteristics of these mesoscale eddies are important because they can greatly affect the fisheries (Kim *et al.*, 2012). There exist actually many observations of such mesoscale eddies in other places: for example, Reddies (Red Sea eddies) (Meschanov & Shapiro, 1998) and Swoddies (Slope water oceanic eddies) (Pingree & Le Cann, 1992; Carton, 2001; Carton *et al.*, 2013).

Idealized models of these vortices have been studied experimentally and numerically with a layered density stratification (Saunders, 1973; Ikeda, 1981; Griffiths & Linden, 1981; Helfrich & Send, 1988; Ripa, 1991; Hopfinger & van Heijst, 1993; Dewar & Killworth, 1995; Killworth *et al.*, 1997; Dewar *et al.*, 1999; Baey & Carton, 2002; Benilov, 2003; Thivolle-Cazat *et al.*, 2005; Aubert *et al.*, 2012; Lahaye & Zeitlin, 2015) as well as in continuously stratified fluids (Dritschel *et al.*, 1999; Reinaud *et al.*, 2003; Nguyen *et al.*, 2012; Lazar *et al.*, 2013b,a; Hua *et al.*, 2013; Dritschel & McKiver, 2015). Saunders (1973) studied experimentally the stability of a vortex produced by releasing a cylindrical volume of fluid into a fluid with a lighter density placed on a turntable rotating at a constant speed. The spreading of the denser fluid at the bottom resulted in an anticyclonic vortex which was stable when the Burger number $Bu = (\delta\rho g/\rho)H/f^2R^2 > 1.8$, where $\delta\rho$ is the density difference between the two fluids, H the height, f the Coriolis parameter and R the radius of the inner cylinder. In contrast, when $Bu < 1.8$, azimuthal disturbances grew on the vortex due to baroclinic instability. The azimuthal wavenumber m scaled like $m \sim 1.8Bu^{-1/2}$, i.e. the wavelength scales like the Rossby deformation radius $R_d = (\delta\rho gH/\rho)^{1/2}/f$, and the smallest wavenumber observed was a $m = 1$ wandering mode of the whole vortex. Similar observations have been later reported by Griffiths & Linden (1981) and Thivolle-Cazat *et al.* (2005) when the inner cylindrical volume of fluid is less dense and has smaller depth than the surrounding fluid. However, the $m = 1$ wandering mode has not been observed for these surface vortices. Numerical simulations performed by Verzicco *et al.* (1997) found good agreement with the results of Griffiths & Linden (1981). Griffiths & Linden (1981) also conducted experiments when a fluid is injected at constant flux into a rotating fluid with a different constant density or with a continuous stratification. In this case, barotropic instability first developed and then baroclinic instability as the anticyclonic vortex grew in size. In the case of continuous stratification, they also observed layers above and below the vortex core that they attributed to the viscous-diffusive instability of McIntyre (1970). A similar instability was observed by Hedstrom & Armi (1988) but non-axisymmetric disturbances were not observed to grow in contrast to Griffiths & Linden (1981). Hedstrom & Armi (1988) have also shown that the aspect ratio and velocity field were in good agreement with the prediction of the lens model of Gill (1981) in quasi-geostrophic fluids. Recently, Aubert *et al.* (2012) and Hassanzadeh *et al.* (2012) have proposed and validated a universal law for the vortex aspect ratio valid in general stratified-rotating fluids which takes into account a density gradient in the vortex core.

Many numerical and theoretical results exist on the stability of axisymmetric vortices for various vortex profiles in one-layer rotating shallow water fluids (Ford, 1994; Stegner & Dritschel, 2000), two-layer quasi-geostrophic fluids (Ikeda, 1981; Helfrich & Send, 1988; Flierl, 1988; Benilov, 2003) or two-layer rotating shallow water fluids for Rossby numbers smaller than unity (Ripa, 1991; Dewar & Killworth, 1995; Killworth *et al.*, 1997; Dewar *et al.*, 1999; Baey & Carton, 2002). In one-layer, vortices with a monotonic potential vorticity may be subjected to a radiative instability (Ford, 1994) while, for isolated vortices, the barotropic shear instability tends to be stabilized as the Burger number Bu decreases (Stegner & Dritschel, 2000). In contrast, two-layer vortices are increasingly unstable to baroclinic instability as Bu decreases. Baroclinic instability is also enhanced (stabilized) when the vortices in each layer are counter-rotating (co-rotating). Recently, Nguyen *et al.* (2012) have conducted a numerical stability analysis of a pancake vortex in continuously stratified quasi-geostrophic fluids. In the case of a Gaussian angular velocity in both radial and vertical directions, they found that the dominant instability when the Burger number $Bu = N^2 \Lambda^2 / f^2 R^2 < 1$ (where N is the Brunt-Väisälä frequency, Λ the half thickness of the vortex and R its radius) is generally a baroclinic instability with an azimuthal wavenumber $m = 2$. However, for very small $Bu < 0.1$, higher azimuthal modes $m > 2$ become dominant. For $Bu > 1$, the dominant mode is a $m = 1$ barotropic mode anti-symmetric with respect to the mid-horizontal plane. Such bending mode is similar to the “internal instability” evidenced by Gent & McWilliams (1986) on columnar isolated vortices in quasi-geostrophic fluids. Yim & Billant (2015) have shown that this instability, which we will call “Gent-McWilliams instability” herein, is due to the presence of a critical point where the angular velocity of the vortex is equal to the phase speed of the disturbances and where the radial gradient of base vorticity is positive. Hua *et al.* (2013) have performed non-linear simulations of the dynamics of a lens-shape vortex in continuously stratified quasi-geostrophic fluids. In addition to the development of the asymmetric disturbances, they evidenced layering in the vicinity of critical levels where the azimuthal phase speed of the disturbances equal the angular velocity of the vortex.

The stability of axisymmetric vortices for larger Rossby numbers has been also investigated (Smyth & McWilliams, 1998; Lazar *et al.*, 2013*b,a*; Lahaye & Zeitlin, 2015; Billant *et al.*, 2004). In the case of a columnar gaussian vortex in inviscid continuously stratified rotating fluids, Smyth & McWilliams (1998) have shown that centrifugal instability becomes dominant over Gent-McWilliams instability and shear instability for sufficiently high Rossby number. Lazar *et al.* (2013*b,a*) studied experimentally and theoretically the stability of vortices in linearly stratified and rotating viscous fluids with respect to the axisymmetric centrifugal instability. Taking into account the leading viscous effects which scale like k^2 for large vertical wavenumber k , they obtained analytic predictions for the most amplified vertical wavenumber and the marginal stability curves in terms of the Burger, Ekman and Rossby numbers. Lahaye & Zeitlin (2015) have investigated the linear stability and non-linear dynamics of anticyclones with a α -Gaussian profile in a two-layer shallow-water model. They have shown that asymmetric centrifugal instabilities become more unstable than the axisymmetric mode as the Rossby number Ro decreases or as the Burger number Bu increases. For small Ro or high Bu , the barotropic shear instability is dominant. Billant *et al.* (2004) have carried out experiments on a

columnar counter-rotating vertical vortex pair in a linearly stratified and rotating fluid. They have shown that the dominant centrifugal instability developing on the anticyclone is non-axisymmetric with an azimuthal wavenumber $m = 1$ for moderate Rossby number and small Froude number.

Recently, Yim & Billant (2016) (hereafter referred as to part 1) have analysed the stability of a Gaussian pancake vortex in continuously stratified non-rotating fluids. Instabilities similar to those of columnar vortices have been observed. Centrifugal instability is almost independent of the aspect ratio due to its short-wavelength nature and occurs when the buoyancy Reynolds number ReF_h^2 is sufficiently large: $ReF_h^2 > 10^3$, where $F_h = \Omega_0/N$ is the Froude number based on the maximum angular velocity Ω_0 and $Re = \Omega_0 R^2/\nu$, where ν is the viscosity. Shear instability can develop when $F_h/\alpha < 0.5$ where $\alpha = \Lambda/R$ is the aspect ratio of the pancake vortex. In addition, instabilities specific to pancake vortices can exist: baroclinic instability when $F_h/\alpha \geq 1.46$ and gravitational instability when $F_h/\alpha \geq 1.5$.

In this paper, we will continue these stability analyses in the case of a stratified-rotating fluid in order to link the infinite Rossby number limit (part 1) to the small Rossby number limit (Nguyen *et al.*, 2012). We show that some instabilities can be traced continuously from the stratified non-rotating limit to the quasi-geostrophic limit while new types of instabilities arise as Ro is varied.

The paper is organized as follows: the stability problem and methods are formulated in §2. The effect of the Rossby number is investigated in §3 while the effects of the other parameters (F_h , α and Re) are studied in §4. In §5, the energetics of some instabilities are analyzed in detail in order to characterize their origin. Conditions of existence for shear instability, Gent-McWilliams instability and baroclinic instability are derived in §6, §7 and §8, respectively. Finally, §9 summarizes the domains of existence of each type of instability in the parameter space (F_h/α , Ro) and (Bu , Ro).

2 Problem formulation

The problem formulation is the same as in part 1 except that the fluid is not only stably stratified but also rotating about the vertical axis at rate $f/2$. For clarity, the main steps of the methods are nevertheless recalled here.

2.1 The base state

As in Nguyen *et al.* (2012) and part 1, we consider an axisymmetric pancake vortex with angular velocity

$$\Omega(r, z) = \Omega_0 e^{-\left(\frac{r^2}{R^2} + \frac{z^2}{\Lambda^2}\right)}, \quad (1)$$

where (r, θ, z) are cylindrical coordinates with z pointing upward, R the radius, Λ the typical half thickness and Ω_0 the maximum angular velocity. The radial and vertical inviscid momentum equations for such steady base flow are

$$-r\Omega^2 - fr\Omega = -\frac{1}{\rho_0} \frac{\partial p_t}{\partial r}, \quad (2)$$

$$0 = -\frac{1}{\rho_0} \frac{\partial p_t}{\partial z} - \frac{g}{\rho_0} \rho_t, \quad (3)$$

where p_t and ρ_t are the total pressure and density, respectively. Combining (2) and (3) gives the thermal-wind equation

$$\frac{\partial \rho_t}{\partial r} = -\frac{\rho_0}{g} \frac{\partial}{\partial z} (r\Omega^2 + fr\Omega), \quad (4)$$

yielding

$$\rho_t = \rho_0 + \bar{\rho}(z) + \rho_b(r, z), \quad (5)$$

with ρ_0 a constant, $\bar{\rho}(z) = -N^2 \rho_0 z / g$ where $N = \sqrt{-g/\rho_0(d\bar{\rho}/dz)}$ is the Brunt-Väisälä frequency which is assumed constant and

$$\rho_b(r, z) = -z \frac{\rho_0}{g} \left(\frac{R}{\Lambda} \right)^2 (\Omega + f) \Omega, \quad (6)$$

is the density field associated with the vortex.

2.2 Linearized Equations

We subject this vortex to infinitesimal perturbations of velocity $\mathbf{u}' = [u'_r, u'_\theta, u'_z]$, pressure p' , and density ρ' written as

$$[u'_r, u'_\theta, u'_z, p', \rho'] = [u_r(r, z), u_\theta(r, z), u_z(r, z), \rho_0 p(r, z), \frac{\rho_0}{g} \rho(r, z)] e^{-i\omega t + im\theta} + \text{c.c.}, \quad (7)$$

where m is the azimuthal wavenumber and $\omega = \omega_r + i\omega_i$, with ω_r the frequency and ω_i the growth rate. The linearized Navier-Stokes equations under the Boussinesq approximations are

$$-i(\omega - m\Omega)u_r - (2\Omega + f)u_\theta = -\frac{\partial p}{\partial r} + \nu \left(\nabla^2 u_r - \frac{1}{r^2} u_r - \frac{2}{r^2} im u_\theta \right), \quad (8)$$

$$-i(\omega - m\Omega)u_\theta + (\zeta + f)u_r + \frac{\partial r\Omega}{\partial z} u_z = -\frac{im}{r} p + \nu \left(\nabla^2 u_\theta - \frac{1}{r^2} u_\theta + \frac{2}{r^2} im u_r \right), \quad (9)$$

$$-i(\omega - m\Omega)u_z = -\frac{\partial p}{\partial z} - \rho + \nu \nabla^2 u_z, \quad (10)$$

$$-i(\omega - m\Omega)\rho + \frac{g}{\rho_0} \frac{\partial \rho_b}{\partial r} u_r + \frac{g}{\rho_0} \frac{\partial \rho_b}{\partial z} u_z = N^2 u_z + \kappa \nabla^2 \rho, \quad (11)$$

$$\frac{1}{r} \frac{\partial r u_r}{\partial r} + \frac{1}{r} im u_\theta + \frac{\partial u_z}{\partial z} = 0, \quad (12)$$

where $\zeta = (1/r)\partial r^2\Omega/\partial r$ is the vertical vorticity, ν the viscosity, κ the diffusivity of the stratifying agent. The viscous and diffusive damping of the base state are neglected in (8)–(12) as classically done in stability analyses (Drazin & Reid, 1981). This assumption is valid as long as the time taken by the perturbations to grow to finite amplitude is small compared to the viscous decay time of the base flow. The problem is governed by five non-dimensional numbers: aspect ratio (α), Froude number (F_h), Rossby number (Ro), Reynolds number (Re), Schmidt number (Sc), defined as follows:

$$\alpha = \frac{\Lambda}{R}, \quad F_h = \frac{\Omega_0}{N}, \quad Ro = \frac{2\Omega_0}{f}, \quad Re = \frac{\Omega_0 R^2}{\nu}, \quad Sc = \frac{\nu}{\kappa}. \quad (13)$$

The Schmidt number is set to $Sc = 1$ throughout the paper. In part 1, the effect of the Schmidt number has been studied and shown to affect only the axisymmetric mode of centrifugal instability. The equations (8) – (12) in the inviscid and non-diffusive limit are non-dimensionalized in appendix A and shown to reduce to the quasi-geostrophic equation when $Ro \ll 1$ and $F_h \ll 1$ whatever the aspect ratio α . For this reason, even if we do not consider here aspect ratios not as small as in the oceans, the quasi-geostrophic regime will be reached for sufficiently small Rossby and Froude numbers.

As explained in part 1, equations (8) – (12) are discretized with finite element methods using FreeFEM++ (Hecht, 2012; Garnaud, 2012) in the domain $0 \leq r \leq R_{\max}$ and $-Z_{\max} \leq z \leq Z_{\max}$. The size is taken as $R_{\max} \geq 10R$ and $Z_{\max} = 5\Lambda$. These sizes are slightly different compared to part 1 because some modes are more sensitive to radial confinement in the presence of background rotation. The mesh is adapted to the base flow so that the mesh is finer ($\sim 0.001R$) inside the vortex core than outside ($\sim 0.1R$). The boundary conditions at $r = 0$ are $u_r = u_\theta = 0$ for $m = 0$, $u_z = p = \rho = 0$ for $m = 1$ and $\mathbf{u} = p = \rho = 0$ for $m \geq 2$. At the other boundaries, $R = R_{\max}$ and $z = \pm Z_{\max}$, all the perturbations are imposed to vanish: $\mathbf{u} = p = \rho = 0$. The matrix version of (8) – (12) built by FreeFEM++ is then solved by means of an iterative Krylov-Schur scheme and a shift-invert method using the SLEPc and PETSc libraries (Hernandez *et al.*, 2005; Garnaud, 2012; Garnaud *et al.*, 2013; Balay *et al.*, 2014; Roman *et al.*, 2015). More details can be found in part 1. The limit $\alpha \rightarrow \infty$ corresponding to a columnar vortex has been solved by means of a Chebyshev collocation spectral method (Antkowiak & Brancher, 2004).

In appendix B, it is shown that the equations (8) – (12) in the quasi-geostrophic and inviscid limits ($Ro \rightarrow 0$, $F_h \rightarrow 0$, $Re = \infty$) can be solved by separation of variables and a shooting method for $Bu = Ro^2 \alpha^2 / (4F_h^2) = 1$. Hence, this particular case has been used as a validation test for the code based on FreeFEM++ and SLEPc. The eigenvalues obtained by the two numerical methods are in good agreement (see appendix B).

3 Overview of the effect of the Rossby number

We first present an overview of the effect of the Rossby number for the azimuthal wavenumbers $m = 0, 1, 2$ starting from the strongly stratified non-rotating limit ($F_h < 1$ and $Ro = \infty$) previously studied in part 1. This will enable us to connect the purely stratified limit to the quasi-geostrophic limit studied by Nguyen *et al.* (2012). Throughout the paper, the exploration of the parameter space will be restricted to the region stable to gravitational instability, i.e. where the total density gradient

$$\frac{\partial \rho_t}{\partial z} = -\frac{\rho_0 N^2}{g} + \frac{\partial \rho_b}{\partial z}, \quad (14)$$

is everywhere negative. This condition can be rewritten in the form

$$\frac{F_h}{\alpha} < c_g(Ro), \quad (15)$$

where c_g is a constant depending on the Rossby number. When $Ro = \infty$, $c_g = e^{3/4}/\sqrt{2} \simeq 1.5$ whereas for $Ro \ll 1$, $c_g = e^{3/4}\sqrt{Ro}/2 \simeq 1.06\sqrt{Ro}$. However,

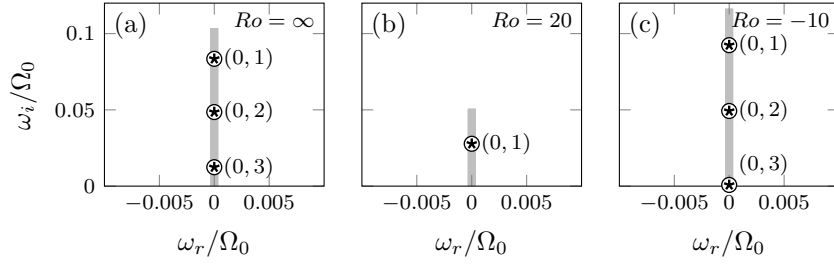


Figure 1: Growth rate (ω_i/Ω_0) and frequency (ω_r/Ω_0) spectra for $m = 0$ for different Rossby numbers Ro : (a) $Ro = \infty$, (b) $Ro = 20$ and (c) $Ro = -10$ for $F_h = 0.5$ and $Re = 10000$. Discrete symbols (\odot : for symmetric and \star for anti-symmetric modes) correspond to pancake vortices for $\alpha = 0.5$ and thick continuous lines (—) correspond to columnar vortices ($\alpha = \infty$).

the constant c_g cannot be expressed analytically for arbitrary Ro . The minimum of the Richardson number

$$Ri = \frac{-\frac{g}{\rho_0} \frac{\partial \rho_t}{\partial z}}{\left(\frac{\partial u_\theta}{\partial z}\right)^2}, \quad (16)$$

is always larger than $1/4$ when the condition (15) is satisfied, meaning that a shear instability due to the vertical shear should not occur in the region stable to gravitational instability (Negretti & Billant, 2013).

3.1 Azimuthal wavenumber $m = 0$

For $m = 0$, it has been found in part 1 that only centrifugal instability exists in stratified fluid when the buoyancy Reynolds number ReF_h^2 is sufficiently high. This remains true when the Rossby number is varied. Figure 1 shows two examples of spectra for $Ro = 20$ and $Ro = -10$ together with the one for $Ro = \infty$, all for the same set of parameters: $\alpha = 0.5$, $F_h = 0.5$ and $Re = 10000$. The unstable modes are shown by symbols and are labelled (m, i) where i is the mode number. For each point, there exist actually two modes with different symmetry with respect to the mid-plane $z = 0$: anti-symmetric (\star) and symmetric (\odot). The maximum growth rate and the number of modes vary with Ro but these variations are consistent with the spectra of the most unstable mode of a columnar vortex for the same Reynolds, Froude and Rossby numbers (grey continuous lines). Some examples of modes are shown in figure 2. The modes are localized inside the region delimited by a dashed line where the Rayleigh discriminant

$$\Phi = \frac{1}{r^3} \frac{\partial}{\partial r} \left(r^4 \left(\Omega + \frac{f}{2} \right)^2 \right) \bigg|_{\rho_t}, \quad (17)$$

is negative. The radial derivative in (17) is taken along constant density surfaces as specified by the generalisation of the Rayleigh criterion to baroclinic vortices (Solberg, 1936; Eliassen & Kleinschmidt, 1957). The minimum of Φ is located on the symmetry plane $z = 0$ whatever Ro but the region of negative Φ has a bean shape for $Ro > \exp(2) = 7.39$ and a croissant shape (extending to the axis at

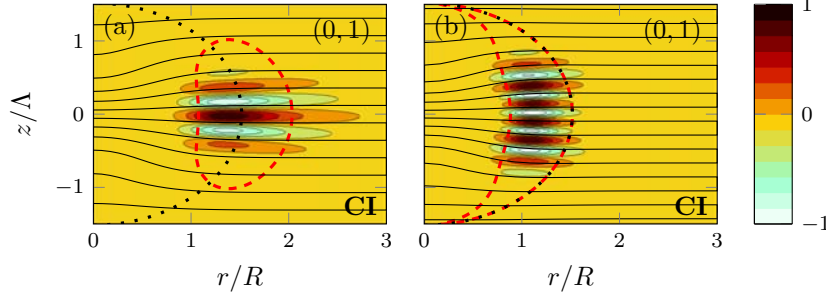


Figure 2: (Colour online) Real part of the radial velocity perturbation $\text{Re}(u_r)$ of centrifugal instability (CI): (a) mode $(0, 1)$ for $Ro = 20$ and (b) mode $(0, 3)$ for $Ro = -10$ indicated in figure 1 ($m = 0, F_h = 0.5, \alpha = 0.5, Re = 10000$). The horizontal lines are isopycnals of the base density field. The dotted line indicates the extension of the base flow by showing the contour where $\Omega = 0.1\Omega_0$. The dashed line indicates the contour where the Rayleigh discriminant Φ vanishes.

$z = \sqrt{\ln(-Ro)}$ for $Ro < -1$. The number of oscillations of the modes along the vertical increases with the mode number but there is always a single oscillation along the radial direction for the parameters of figure 1. The variation of the growth rate of the most unstable mode as a function of Ro for $\alpha = 0.5, F_h = 0.5$ and $Re = 10000$ is summarized in figure 3 (dashed line with circles). Centrifugal instability is stabilized for small Rossby number in the range $-3.5 < Ro < 17$. A similar evolution of the maximum growth rate is observed for a columnar vortex (grey continuous line). As shown in part 1, the growth rate of centrifugal instability can be predicted using the asymptotic formula of Billant & Gallaire (2005) for large axial wavenumber k for a columnar vortex with the addition of the leading viscous term as in Lazar *et al.* (2013b):

$$\omega = \omega^{(0)} - \frac{\omega^{(1)}N}{k} - i\nu k^2, \quad (18)$$

where

$$\omega^{(0)} = m\Omega(r_0) + i\sqrt{-\phi(r_0)}, \quad (19)$$

$$\omega^{(1)} = \frac{n i}{2\sqrt{2}} \sqrt{\frac{\phi''(r_0) - 2m^2\Omega'(r_0)^2 + 2im\sqrt{-\phi(r_0)}\Omega''(r_0)}{-\phi(r_0)}} \sqrt{1 - \frac{\phi(r_0)}{N^2}}, \quad (20)$$

with n a non-negative integer, $\phi = (2\Omega + f)(\zeta + f)$ and r_0 is given by

$$\phi'(r_0) = -2im\Omega'(r_0)\sqrt{-\phi(r_0)}. \quad (21)$$

The maximum growth rate predicted by (18) for $F_h = 0.5$ and $Re = 10000$ is shown by the dashed grey line in figure 3. It is close to the maximum growth rate for both columnar and pancake vortices. We can remark that the maximum growth rate for $F_h = 0.5$ and $Re = 10000$ is approximately three times smaller than the theoretical upper limit for the growth rate of centrifugal instability which is $\sqrt{-\min(\phi)}$ for $m = 0$ (solid line in figure 3) and which is attained in the limit $k \rightarrow \infty$ and $\nu \rightarrow 0$. Note that $\min(\phi) = \min(\Phi)$ since Φ is minimum on the symmetry plane $z = 0$.

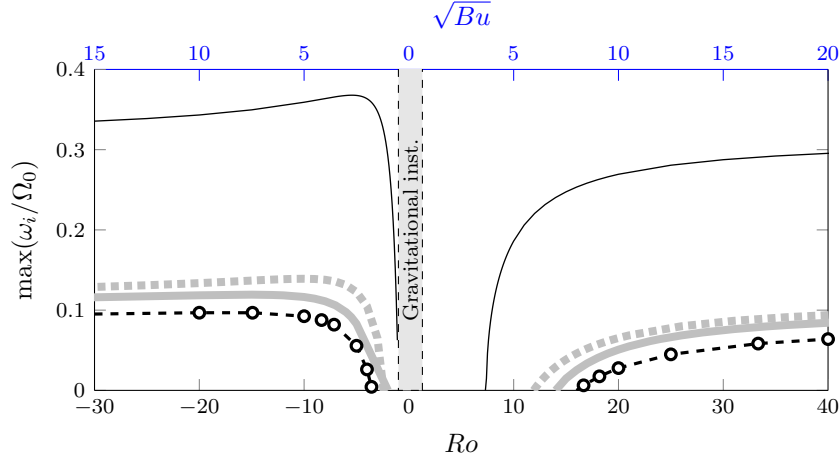


Figure 3: (Colour online) Maximum growth rate of centrifugal instability for $m = 0$ as a function of Ro for a pancake vortex for $\alpha = 0.5$ ($-\circ-$) and a columnar vortex ($---$) for $F_h = 0.5$ and $Re = 10000$. The dashed grey line ($----$) shows the maximum of the asymptotic growth rate (18) and the solid line ($---$) shows the upper limit for the growth rate of centrifugal instability for $m = 0$: $\sqrt{-\min(\phi)}$. The vertical shaded region is the region unstable to gravitational instability. The upper x -axis indicates the corresponding value of square root of the Burger number \sqrt{Bu} .

3.2 Azimuthal wavenumber $m = 1$

An example of spectrum for $m = 1$ for a large Rossby number $Ro = 20$ and $\alpha = 0.5$, $F_h = 0.5$ and $Re = 10000$ is displayed in figure 4b. The spectrum of a columnar vortex for the same parameter is also shown by a continuous grey line for comparison. These spectra are qualitatively similar to those for $Ro = \infty$ (shown in figure 4a for reference) in which three types of modes have been identified in part 1. From this basis, we can easily classify the different modes in figure 4b. The series of modes ((1,1)–(1,4), (1,6)–(1,8)) correspond to centrifugal instability. The eigenmodes differ again by the number of oscillations along the vertical (compare modes (1,1) and (1,3) in figure 5) but they have all a single oscillation along the radial direction. They are localized near the region where Φ is negative and they tend to be aligned along the base isopycnals (figure 5a,b). The mode (1,5) in figure 4b corresponds to a mixed Gent-McWilliams-centrifugal instability since it exhibits both the characteristics of centrifugal and Gent-McWilliams instabilities (figure 5c). The latter instability, which is also called internal instability, bends the vortex and is due to the presence of a critical layer where $\Omega = \omega_r$ and where the vertical vorticity radial gradient is positive (Gent & McWilliams, 1986; Smyth & McWilliams, 1998; Yim & Billant, 2015). The mode (1,9) is almost neutral with zero frequency for large Re . Its radial velocity perturbation (figure 5d) is almost identical to the angular velocity of the base flow, implying that it displaces the vortex without deforming it. As shown in part 1, this mode corresponds to the displacement mode originating from the translational invariance. In §4.1, it will be shown that the instability of the displacement mode is due to viscous effects.

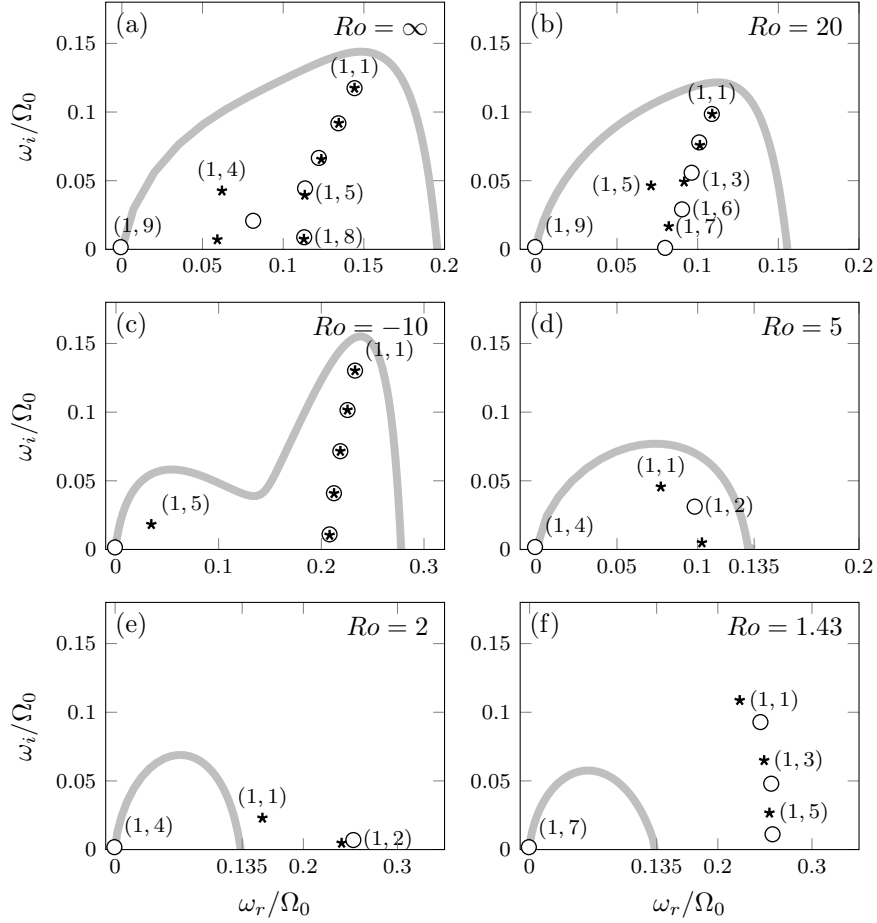


Figure 4: Growth rate (ω_i/Ω_0) and frequency (ω_r/Ω_0) spectra for $m = 1$ for different Rossby numbers Ro : (a) $Ro = \infty$, (b) $Ro = 20$, (c) $Ro = -10$ (d) $Ro = 5$, (e) $Ro = 2$ and (f) $Ro = 1.43$ for $F_h = 0.5$ and $Re = 10000$. Discrete symbols (\circ : for symmetric and \star for anti-symmetric modes) correspond to pancake vortices for $\alpha = 0.5$ and thick continuous lines (—) correspond to columnar vortices ($\alpha = \infty$).

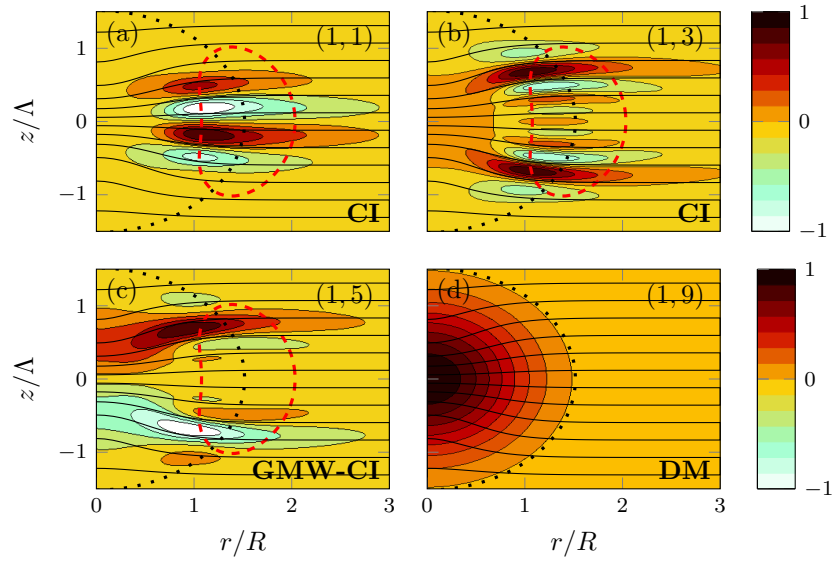


Figure 5: (Colour online) Real part of the radial velocity perturbation $\text{Re}(u_r)$ of centrifugal instability (CI) (a) mode (1,1) and (b) mode (1,3), (c) mixed Gent-McWilliams-centrifugal instability (GMW-CI) (1,5) and (d) the displacement mode (DM) (1,9) for $Ro = 20$ (figure 4b) ($m = 1, \alpha = 0.5, F_h = 0.5, Re = 10000$). The horizontal lines are isopycnals. The dotted line indicates the extension of the base flow by showing the contour where $\Omega = 0.1\Omega_0$. The dashed line indicates the contour where the Rayleigh discriminant Φ vanishes.

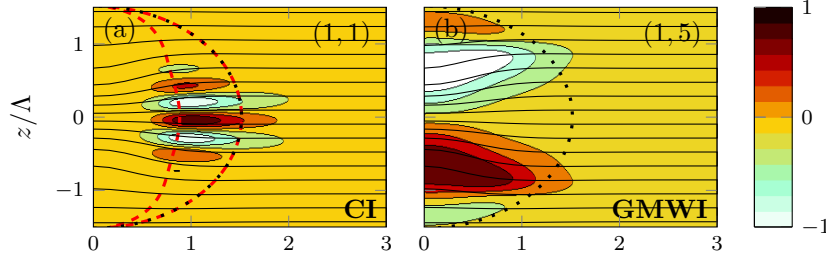


Figure 6: (Colour online) Real part of the radial velocity perturbation $\text{Re}(u_r)$ of (a) centrifugal instability (1, 1) and (b) Gent-McWilliams instability (GMWI) (1, 5) for $Ro = -10$ (figure 4c) ($m = 1, \alpha = 0.5, F_h = 0.5, Re = 10000$). The horizontal lines are isopycnals. The dotted line indicates the extension of the base flow by showing the contour where $\Omega = 0.1\Omega_0$. The dashed line indicates the contour where the Rayleigh discriminant Φ vanishes.

A similar spectrum is observed for $Ro = -10$ (figure 4c) except that there is a clear separation between centrifugal and Gent-McWilliams instabilities. This is similar to the columnar vortex case (grey solid line) where Gent-McWilliams instability and centrifugal instability correspond to two distinct growth rate peaks for negative Rossby numbers in contrast to positive Rossby numbers (Yim & Billant, 2015). The structure of centrifugal instabilities (figure 6a) is similar to those for $Ro = 20$ (figure 5a,b). Gent-McWilliams instability (figure 6b) is localized in the vortex core and corresponds more clearly to a bending of the vortex as a whole than for $Ro = 20$ (figure 5c) where the mixed Gent-McWilliams-centrifugal mode tends to concentrate at the top and bottom of the pancake vortex.

When the absolute value of the Rossby number is further decreased, centrifugal instability disappears since $\Phi > 0$ everywhere when $-1 \leq Ro \leq 7.39$ and only Gent-McWilliams instability remains as exemplified in figure 4d for $Ro = 5$. In this case, there are three unstable Gent-McWilliams modes and the first two are displayed in figure 7. The first one (figure 7a) is similar to the one previously shown in figure 6b for $Ro = -10$ while the second one exhibits one more oscillation along the vertical and is thus symmetric (figure 7b). There is still also the displacement mode ((1,4) in figure 4d) with a very weak frequency and growth rate. All these modes are close to the spectrum of a columnar vortex shown by the grey solid line (figure 4d). The maximum frequency of the unstable branch of the columnar vortex is $\omega_r = \Omega_0 e^{-2} = 0.135\Omega_0$. This corresponds to the maximum frequency for which the gradient of the vertical vorticity $\zeta'(r_c)$ is positive at the critical radius r_c where $\Omega(r_c) = \omega_r$.

So far, all the unstable modes observed for a pancake vortex derive from those for a columnar vortex. However, when the Rossby number is further decreased to $Ro = 2$ (figure 4e) and then to $Ro = 1.43$ (figure 4f), all the unstable modes for pancake vortices have no counterparts in columnar vortices except the displacement mode near the origin ((1,4) in figure 4e and (1,7) in figure 4f). For $Ro = 2$ (figure 4e), the most unstable mode (1,1) has a frequency larger than $0.135\Omega_0$ but is still close to the spectra of the columnar vortex. The structure of this mode (figure 8a) is similar to Gent-McWilliams instability for

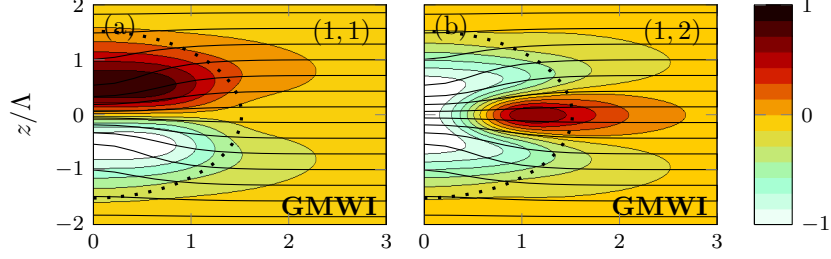


Figure 7: (Colour online) Real part of the radial velocity perturbation $\text{Re}(u_r)$ of Gent-McWilliams instability (GMWI): (a) mode $(1, 1)$ and (b) mode $(1, 2)$ for $Ro = 5$ (figure 4d) ($m = 1, \alpha = 0.5, F_h = 0.5, Re = 10000$). The horizontal lines are isopycnals. The dotted line indicates the extension of the base flow by showing the contour where $\Omega = 0.1\Omega_0$.

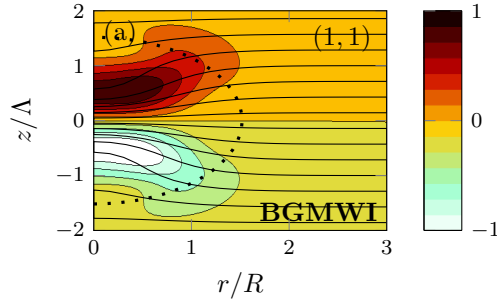


Figure 8: (Colour online) Real part of the radial velocity perturbation $\text{Re}(u_r)$ of the mixed baroclinic-Gent-McWilliams instability (BGMWI): mode $(1, 1)$ for $Ro = 2$ (figure 4e) ($m = 1, \alpha = 0.5, F_h = 0.5, Re = 10000$). The horizontal lines are isopycnals. The dotted line indicates the extension of the base flow by showing the contour where $\Omega = 0.1\Omega_0$.

$Ro = 5$ (figure 7a) but it tends to be distorted near $r = R$. In section 5, we will show that the energy source of this mode is the potential energy of the base flow instead of the kinetic energy. For this reason, we shall call it mixed baroclinic-Gent-McWilliams instability. Two other modes start also to be observed near the frequency $\omega_r = 0.25\Omega_0$ (figure 4e) but they are weakly unstable. In contrast, for $Ro = 1.43$ (figure 4f), they are many modes around this frequency and their growth rate is much larger. The leading mode (1,1) corresponds in fact to baroclinic-Gent-McWilliams mode whose frequency and growth rate have increased until merging with the series of modes aligned near the frequency $\omega_r = 0.25\Omega_0$. A selection of these modes are depicted in figure 9. The first mode (1,1) shows some similarities with the one for $Ro = 2$ (figure 8) but it is clearly more concentrated in the vortex core $r/R_0 \leq 0.5$ and is maximum at a slightly higher vertical level $z/\Lambda = \pm 0.7$. The next modes are similar but exhibit more radial oscillations (figure 9b,c,d) with still two vertical oscillations, i.e. one per half vertical plane. Similar modes have been observed in stratified non-rotating fluids (part 1) when the isopycnal deformations are sufficiently strong and have been attributed to baroclinic instability. The isopycnals are indeed more and more distorted when the Rossby number decreases for given aspect ratio and Froude number. The isopycnals even overturn, i.e. $\max(\partial\rho_t/\partial z) > 0$, when $Ro \leq 1.3$ for $\alpha = 0.5$ and $F_h = 0.5$. In quasi-geostrophic fluids, a necessary condition for baroclinic instability is the sign change of the potential vorticity gradient along isopycnal (Charney & Stern, 1962; Eliassen, 1983; Hoskins *et al.*, 1985; Ménesguen *et al.*, 2012b):

$$\left. \frac{\partial \Pi}{\partial r} \right|_{\rho_t} = \frac{\partial \Pi}{\partial r} - \frac{\partial \Pi}{\partial z} \frac{\frac{\partial \rho_t}{\partial r}}{\frac{\partial \rho_t}{\partial z}} = 0, \quad (22)$$

where $\Pi = (\zeta + f)\partial\rho_t/\partial z - r\partial\Omega/\partial z\partial\rho_t/\partial r$ is the potential vorticity of the base flow. The double dotted dashed line in figure 9 shows where $\partial\Pi/\partial r|_{\rho_t} = 0$. As can be seen, the modes develop in the vicinity of this line suggesting that they are due to baroclinic instability. In this respect, the leading mode (1,1) (figure 9a) is not different from the following modes (figure 9b,c,d) and could be equally classified as baroclinic. However, we will continue to call it baroclinic-Gent-McWilliams mode since it derives continuously from Gent-McWilliams instability as Ro increases. A detailed study of these baroclinic modes will be conducted in §8.

The effect of the Rossby number on the growth rate and frequency of the most unstable modes of each instability for $m = 1$ is summarized in figure 10. As already seen for $m = 0$, centrifugal instability (dashed line with circles) is stabilized for small negative $Ro \gtrsim -2$. For positive Rossby number, centrifugal instability transforms continuously into the Gent-McWilliams instability (dashed line with filled triangle) when $Ro \lesssim 7$ (Yim & Billant, 2015). The growth rate of the mixed Gent-McWilliams-centrifugal instability (dashed line with open triangle) is almost constant for large Rossby number. For negative Rossby number, Gent-McWilliams instability stabilizes around $Ro \sim -2$ like centrifugal instability. For positive Rossby number, the growth rate of Gent-McWilliams instability decreases as the Rossby number decreases and becomes minimum for $Ro = 2$ corresponding to a Burger number $Bu = (\alpha Ro/2F_h)^2 \equiv (N\Lambda/fR)^2$ around unity as indicated in the upper x axis in figure 10. Below this Rossby number, the frequency (figure 10b) increases beyond the cutoff frequency $\omega_r = 0.135\Omega_0$ above

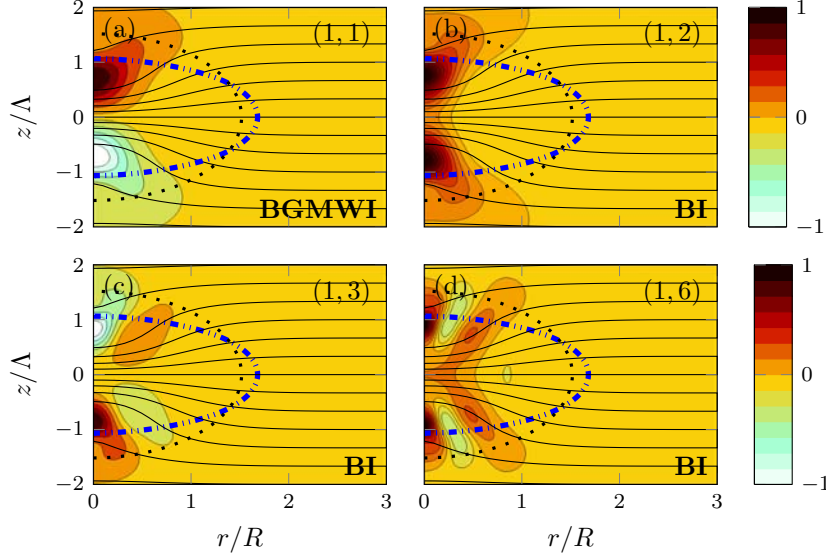


Figure 9: (Colour online) Real part of the radial velocity perturbation $\text{Re}(u_r)$ of the (a) mode (1, 1), (b) mode (1, 2), (c) mode (1, 3) and (d) mode (1, 6) for $Ro = 1.43$ (figure 4f) ($m = 1, \alpha = 0.5, F_h = 0.5, Re = 10000$). The horizontal lines are isopycnals. The dotted line indicates the extension of the base flow by showing the contour where $\Omega = 0.1\Omega_0$. The double dotted dashed line ($\cdot-\cdot-\cdot$) shows where the isopycnal potential vorticity gradient (22) changes sign.

which Gent-McWilliams instability no longer exists in the case of a columnar vortex (Yim & Billant, 2015). Simultaneously, the growth rate re-increases and the instability becomes a mixed baroclinic-Gent-McWilliams instability (dashed line with star). For smaller Rossby number, the instability merges with the pure baroclinic instability (dashed line with diamond) with a growth rate increasing dramatically as Ro decreases. However, the frequency saturates at $\omega_r \simeq 0.25\Omega_0$. The growth rate of the displacement mode (dashed line with square) remains very low for any Rossby number.

Similar results have been obtained by Nguyen *et al.* (2012) in quasi-geostrophic fluids except that centrifugal instability is absent since $Ro \ll 1$. Thus, they have reported for $m = 1$ only two modes that they distinguish by their symmetry: a symmetric and an anti-symmetric mode. When the Burger number is of order unity or larger, the symmetric mode corresponds to the displacement mode herein and the anti-symmetric mode is similar to Gent-McWilliams most unstable mode. In contrast, when Bu is small, the symmetric and anti-symmetric modes correspond to the leading baroclinic modes herein (BGMWI or BI depending on Bu). The growth rate of the anti-symmetric mode is minimum for $Bu = 1$ like in figure 10 when the transition between Gent-McWilliams and baroclinic-Gent-McWilliams instabilities occurs.

Finally, figure 11 shows that the maximum growth rate and corresponding frequency of centrifugal instability for pancake (dashed line with circle) and columnar (grey continuous line) vortices are close. The maximum growth rate and associated frequency predicted by (18) is also represented by a dashed

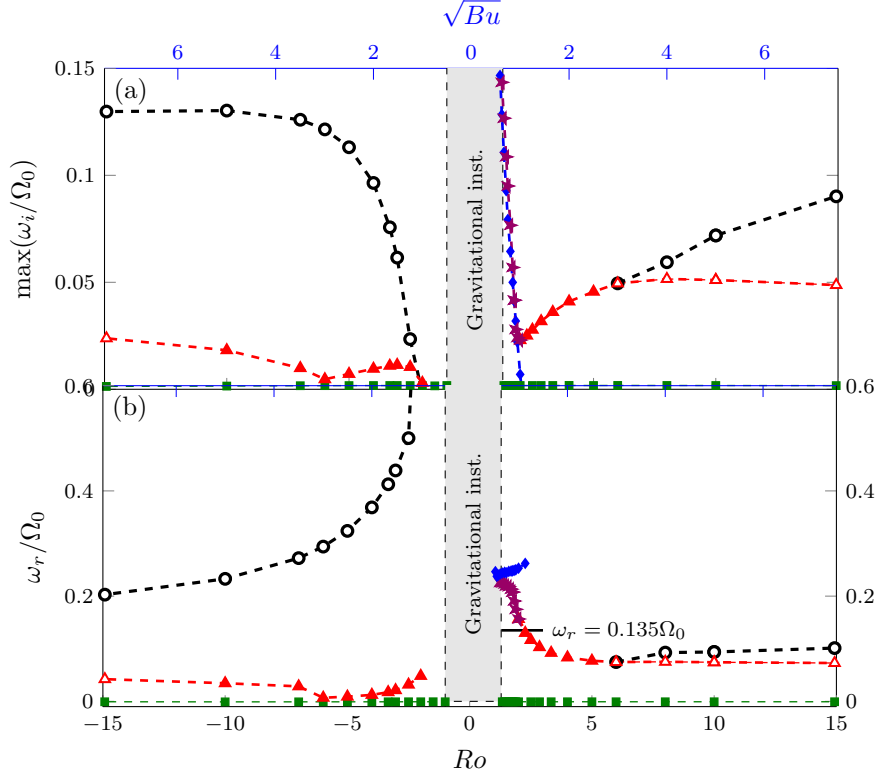


Figure 10: (Colour online) (a) Maximum growth rates and (b) corresponding frequencies of the different types of instability as a function of Ro for $m = 1$, $\alpha = 0.5$, $F_h = 0.5$ and $Re = 10000$: centrifugal instability - \circ -, displacement mode - \square -, Gent-McWilliams instability - \triangle -, mixed Gent-McWilliams-centrifugal instability - \diamond -, mixed baroclinic Gent-McWilliams instability - \star - and baroclinic instability - \diamond -. The upper x axis indicates the corresponding value of the square root of the Burger number \sqrt{Bu} . The shaded region is gravitationally unstable.

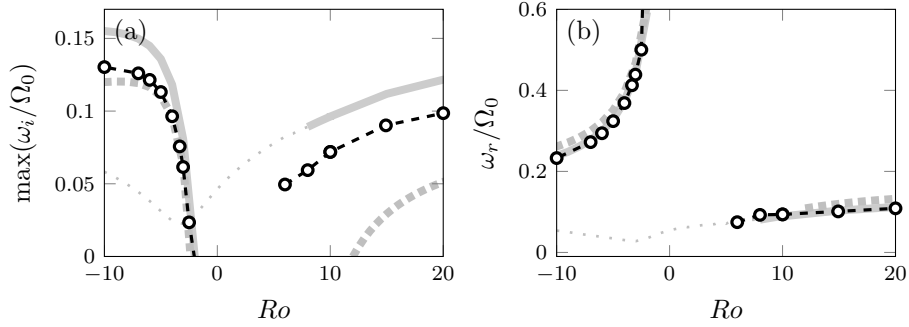


Figure 11: (a) Maximum growth rate and (b) corresponding frequency of centrifugal instability (—) for columnar (thick continuous lines) and pancake ($\alpha = 0.5$) (—○—) vortices as a function of Ro for $m = 1$, $F_h = 0.5$ and $Re = 10000$. The dashed grey line shows the maximum of the asymptotic growth rate (18). The dotted line indicates Gent-McWilliams instability.

line. It underestimates the observed growth rate of both pancake and columnar vortices for positive Rossby number. This discrepancy comes from the smooth transition between Gent-McWilliams and centrifugal instabilities as Ro varies.

In summary, for $m = 1$, baroclinic-Gent-McWilliams instability dominates when Ro is small and centrifugal instability takes over when Ro is large. In between, there exists Gent-McWilliams instability for positive Ro . For negative Ro , centrifugal instability is always dominant. Although, only one particular set of parameters ($\alpha = 0.5$, $F_h = 0.5$ and $Re = 10000$) has been presented, we shall see in section 4 that this picture is typical of other parameter combinations in the strongly stratified regime with moderate and strong rotation.

3.3 Azimuthal wavenumber $m = 2$

Finally, we present the effect of the Rossby number on the stability of the azimuthal wavenumber $m = 2$ for the set of parameters: $\alpha = 1.2$, $F_h = 0.5$ and $Re = 10000$. Note that the aspect ratio is changed compared to $m = 0$ and $m = 1$ in order to show more typical examples of spectra. In the strongly stratified non-rotating case (part 1), two instabilities have been found: centrifugal instability for sufficiently large buoyancy Reynolds number ReF_h^2 and shear instability when $F_h/\alpha \leq 0.5$. These correspond to the modes (2,1)–(2,2) and (2,3), respectively in figure 12a. When the Rossby number is decreased, a scenario similar to the one described for $m = 1$ occurs. Centrifugal instability becomes less dominant for moderate Rossby number (see figure 12b for $Ro = 20$) and disappears for small Rossby number (see figure 12c for $Ro = 0.8$) since $\Phi > 0$ for $-1 < Ro < 7.39$. An example of the structure of a centrifugal mode for $Ro = 20$ is depicted in figure 13b. In contrast, baroclinic instability appears for small Rossby number (modes (2,1)–(2,4) in figure 12d for $Ro = 0.25$). As for $m = 1$ (figure 9), baroclinic modes differ by the number of oscillations in the radial direction and by their symmetry with respect to the mid-plane $z = 0$ (not shown).

For all the Rossby numbers presented in figure 12, shear instability remains present around the same frequency in the vicinity of the shear instability branch

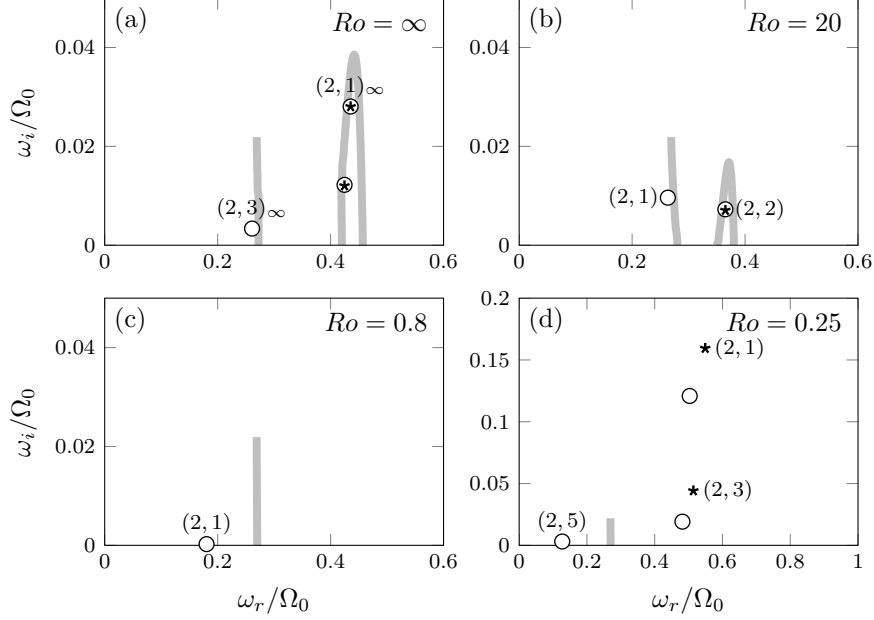


Figure 12: Growth rate (ω_i/Ω_0) and frequency (ω_r/Ω_0) spectra for $m = 2$ for different Rossby numbers Ro : (a) $Ro = \infty$, (b) $Ro = 20$, (c) $Ro = 0.8$ and (d) $Ro = 0.25$ for $F_h = 0.5$ and $Re = 10000$. Discrete symbols (\circ : for symmetric and \star for anti-symmetric modes) correspond to pancake vortices for $\alpha = 1.2$ and thick continuous lines (—) correspond to columnar vortices ($\alpha = \infty$).

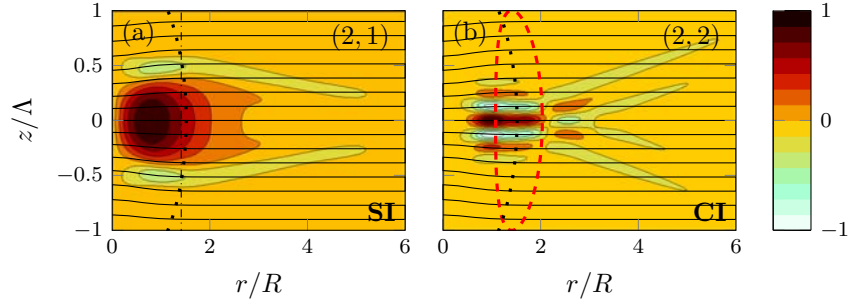


Figure 13: (Colour online) Real part of the radial velocity perturbation $\text{Re}(u_r)$ of (a) shear instability (SI) $(2,1)$ and (b) centrifugal instability (CI) $(2,2)$ for $Ro = 20$ (figure 12b) ($m = 2, \alpha = 1.2, F_h = 0.5, Re = 10000$). The horizontal lines are isopycnals. The dotted line indicates the extension of the base flow by showing the contour where $\Omega = 0.1\Omega_0$. The dash dotted line in (a) shows the inflection radius r_I where $\zeta'(r_I) = 0$. The dashed line in (b) indicates the contour where the Rayleigh discriminant Φ vanishes.

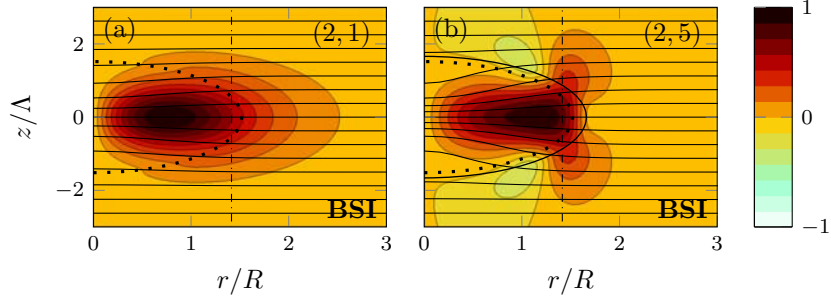


Figure 14: (Colour online) Real part of the radial velocity perturbation $\text{Re}(u_r)$ of the mixed baroclinic-shear instability (BSI) (a) mode (2, 1) for $Ro = 0.8$ (figure 12c) and (b) mode (2, 5) for $Ro = 0.25$ (figure 12d) ($m = 2, \alpha = 1.2, F_h = 0.5, Re = 10000$). The horizontal lines are isopycnals. The dotted line indicates the extension of the base flow by showing the contour where $\Omega = 0.1\Omega_0$. The dash dotted line shows the inflection radius r_I where $\zeta'(r_I) = 0$. The solid line in (b) show the critical layer where $\omega_r = m\Omega(r, z)$.

of the columnar vortex (grey continuous line near $\omega_r/\Omega_0 = 0.26$). However, its growth rate for the pancake vortex varies with Ro while the maximum growth rate for the columnar vortex is independent of the Rossby number since the dominant mode is two-dimensional. The shape of the shear instability mode also varies somewhat with the Rossby number (see figure 13a for $Ro = 20$, figure 14 for $Ro = 0.8$ and $Ro = 0.25$). The mode for $Ro = 20$ is almost identical to the one found for $Ro = \infty$ (part 1). The mode for $Ro = 0.25$ (figure 14b) is similar but extends vertically around $r/R = r_I/R = 1.4$ where r_I is the inflection point where $\partial\zeta(r, z)/\partial r = 0$ at $z = 0$. A similar mode has been found by Nguyen *et al.* (2012) in quasi-geostrophic fluids. They argued that this mode originates from a baroclinic instability induced by the critical layer where $\omega_r = m\Omega$. As can be seen in figure 14b, the mode tends indeed to be distorted along the critical layer (shown by a solid line). However, figure 12 shows that this mode derives continuously from shear instability. In addition, we will show in section 5 that the energy source of this instability is the potential energy of the base flow instead of the kinetic energy. For this reason, we will call here this instability: mixed baroclinic-shear instability.

Figure 15 outlines the effect of the Rossby number on the maximum growth rate and associated frequency of each instability. Centrifugal instability (dashed line with open circle) is stabilized for $-3 \leq Ro \leq 17$ and is stronger for negative Rossby number than for positive ones as already observed for $m = 0$ and $m = 1$. Strikingly, the opposite behaviour is observed for shear instability (dashed line with filled circle): it tends to be enhanced for moderate positive Rossby numbers and attenuated for finite negative Rossby numbers. However, the growth rate of shear instability decreases to zero as Ro decreases from $Ro = 7$ to $Ro = 1$. Below $Ro = 1$ (which corresponds to $Bu = 1$ as indicated in the upper x axis), it starts to re-increase but the instability is then of the mixed type: baroclinic-shear instability. Such growth rate minimum for $Bu \simeq 1$ is consistent with the results of Nguyen *et al.* (2012). This mixed instability exists down to $Ro = -0.6$ while the classical shear instability reappears for $Ro \simeq -23$. Baroclinic instability

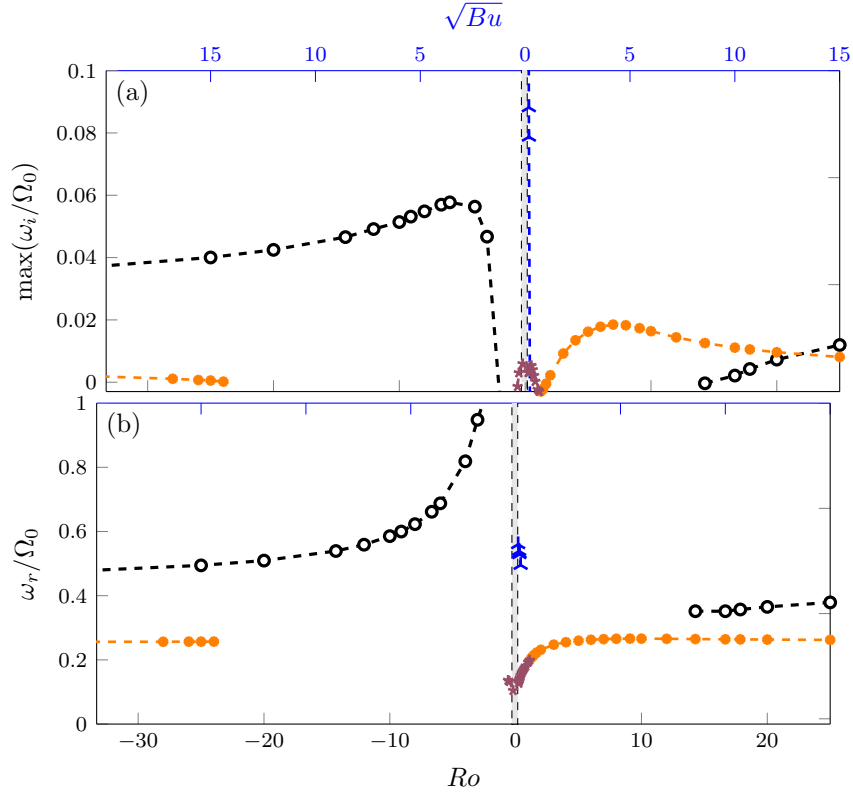


Figure 15: (Colour online) (a) Maximum growth rates and (b) corresponding frequencies of the different types of instabilities as a function of Ro for $m = 2, \alpha = 1.2, F_h = 0.5$ and $Re = 10000$: centrifugal instability - \circ -, shear instability - \bullet -, baroclinic-shear instability - $*$ - and baroclinic instability - Δ -. The upper x axis indicates the corresponding value of the square root of the Burger number \sqrt{Bu} . The shaded region is gravitationally unstable.

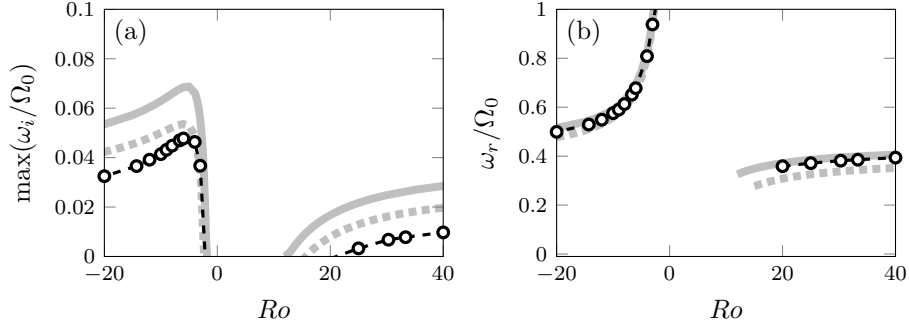


Figure 16: (a) Maximum growth rates and (b) corresponding frequencies of centrifugal instability for columnar (thick continuous lines, —) and pancake ($\alpha = 1.2$) (thick dashed lines, $\text{--}\circ\text{--}$) vortices for $m = 2$, $F_h = 0.5$ and $Re = 10000$. The dashed grey line (---) shows the maximum of the asymptotic growth rate (18).

co-exists for small Rossby numbers in the range $0 \leq Ro \leq 0.4$. Its growth rate becomes very high as soon as the Rossby number threshold is crossed but its frequency remains almost constant $\omega_r \simeq 0.5\Omega_0$ (figure 15b).

In figure 16, the maximum growth rate and associated frequency of centrifugal instability for $m = 2$ for a pancake vortex is further compared to the one for a columnar vortex. As already seen for $m = 0$ and $m = 1$, they are close and in reasonable agreement with the asymptotic formula (18).

4 Effects of the other parameters for a fixed Rossby number

In this section, we now fix the Rossby number and vary the other control parameters: Reynolds number, Re , aspect ratio, α and Froude number, F_h . In most of the section, the Rossby number will be fixed to $Ro = 1.25$ but smaller values will be also investigated at the end. For these values of the Rossby number, centrifugal instability is not active but all the other instabilities seen in section 3 may occur for some parameter combinations. Only the most unstable mode for each type of instability will be studied and the two azimuthal wavenumbers $m = 1$ and $m = 2$ will be presented together ($m = 0$ is stable for $Ro \leq 1.25$). We will not study further centrifugal instability since it has the same characteristics as for columnar vortices and is almost independent of the aspect ratio of the vortex. For $Ro = \infty$ (part 1), its growth rate has been shown to depend mostly on ReF_h^2 and this is expected to remain true for any given finite Ro .

4.1 Effect of the Reynolds number

Figure 17 shows the effect of the Reynolds number on the maximum growth rate and associated frequency for $\alpha = 0.5$, $F_h = 0.3$ and $Ro = 1.25$. For these parameters, only Gent-McWilliams instability and displacement mode are unstable for $m = 1$ while only baroclinic-shear instability is unstable for $m = 2$.

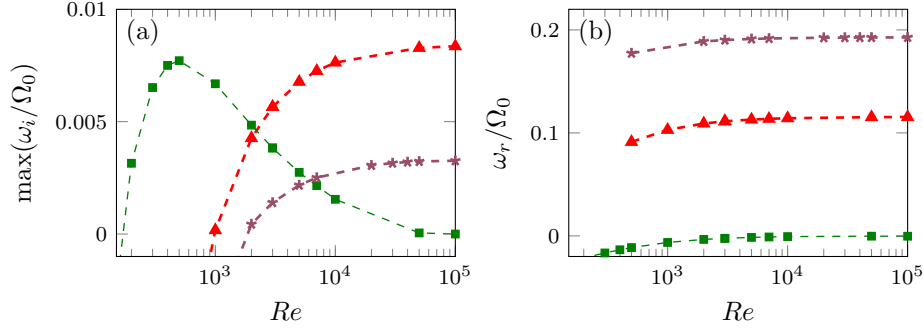


Figure 17: (Colour online) (a) Maximum growth rates and (b) corresponding frequencies as a function of the Reynolds number Re for Gent-McWilliams instability (-▲-), displacement mode (-■-) for $m = 1$ and baroclinic-shear instability (-*-) for $m = 2$ for $\alpha = 0.5$, $F_h = 0.3$, and $Ro = 1.25$.

The growth rates of Gent-McWilliams instability (dashed line with triangles) and baroclinic-shear instability (dashed line with stars) asymptote to a constant value for large Re and decreases to zero for $Re \simeq 1000$ and $Re \simeq 2000$, respectively. Surprisingly, the growth rate of the displacement mode (dashed line with squares) first increases when the Reynolds number decreases. Thereby, it is most unstable for a finite Reynolds number $Re \simeq 500$. The instability of the displacement mode is therefore of viscous origin. A similar viscous instability of the displacement mode of a columnar vortex exists in stratified-rotating fluids (Billant, 2010; Riedinger *et al.*, 2010). Further analysis would be necessary to explain its detailed mechanism. In summary, for the given parameters $\alpha = 0.5$, $F_h = 0.5$ and $Ro = 1.25$, the $m = 1$ displacement instability is dominant for $Re < 2000$ while the $m = 1$ Gent-McWilliams instability is dominant for higher Re .

4.2 Effect of the Froude number

The Froude number is now varied for $Re = 10000$ still for $\alpha = 0.5$ and $Ro = 1.25$ (figure 18). The displacement mode (dashed line with squares) keeps a very low growth rate and frequency independently of the Froude number. In contrast, the growth rate of Gent-McWilliams instability (dashed line with triangles) fluctuates with F_h : it exhibits two successive maxima as the Froude number increases before increasing widely when it transforms into the mixed baroclinic-Gent-McWilliams instability. The structure of the mode for some selected Froude numbers is displayed in figure 19. For $F_h = 0.05$, the mode exhibits five oscillations along the vertical and is symmetric while for $F_h = 0.2$, it has only two oscillations occupying the whole pancake vortex and is anti-symmetric as seen before (see figure 7a). This change of structure explains why there is a slight frequency jump in figure 18b (dashed line with triangles) and two growth rate maxima (figure 18a). For $F_h = 0.4$ (figure 19c), the mode is of mixed type: baroclinic-Gent-McWilliams with a frequency above the cutoff $\omega_r = 0.135\Omega_0$ of Gent-McWilliams instability and slightly below the frequency $\omega_r = 0.25\Omega_0$ of baroclinic instability (figure 18b).

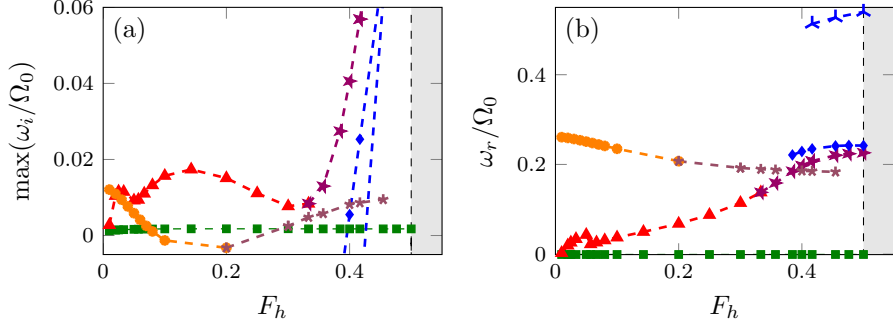


Figure 18: (Colour online) (a) Maximum growth rates and (b) corresponding frequencies as a function of the Froude number F_h for $\alpha = 0.5$, $Ro = 1.25$ and $Re = 10000$ of the different instabilities: displacement mode (-■-); Gent-McWilliams instability (-▲-); baroclinic-Gent-McWilliams instability (-✱-); baroclinic instability (-◆-) for $m = 1$; shear instability (-○-); baroclinic-shear instability (-✱-) and baroclinic instability for $m = 2$ (-✱-). The shaded area indicates the gravitationally unstable region.

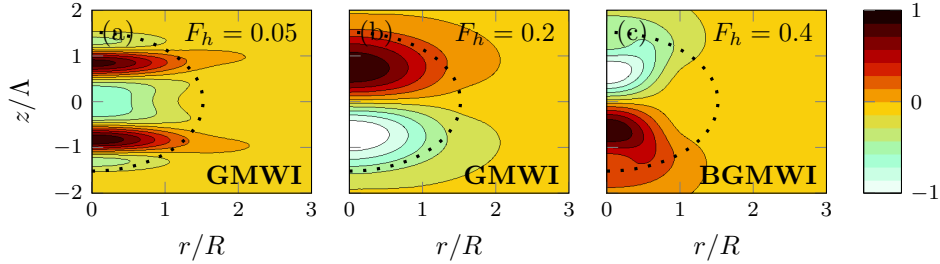


Figure 19: (Colour online) Real part of the radial velocity perturbation $\text{Re}(u_r)$ of the most unstable mode for different Froude numbers: Gent-McWilliams instability for (a) $F_h = 0.05$ and (b) $F_h = 0.2$, and (c) mixed baroclinic-Gent-McWilliams instability for $F_h = 0.4$ for $m = 1$, $\alpha = 0.5$, $Ro = 1.25$, and $Re = 10000$. The dotted line indicates the extension of the base flow by showing the contour where $\Omega = 0.1\Omega_0$.

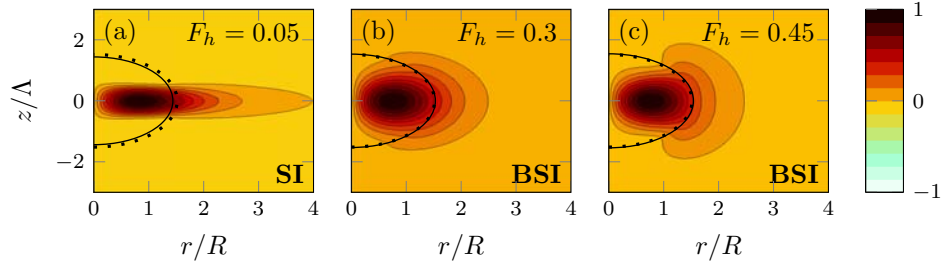


Figure 20: (Colour online) Real part of the radial velocity perturbation $\text{Re}(u_r)$ of the most unstable modes for different Froude numbers: shear instability for (a) $F_h = 0.05$ and mixed baroclinic-shear instability for (b) $F_h = 0.3$ and (c) $F_h = 0.45$ for $m = 2, \alpha = 0.5, Ro = 1.25$ and $Re = 10000$. The dotted line indicates the extension of the base flow by showing the contour where $\Omega = 0.1\Omega_0$. The solid line (—) is the critical layer (r_c, z_c) where $m\Omega(r_c, z_c) = \omega_r$.

Shear instability for $m = 2$ (dashed line with filled circles in figure 18) is most unstable as $F_h \rightarrow 0$ and stabilizes for $F_h \simeq 0.1$. However, it becomes unstable again for $F_h \geq 0.3$ but under the mixed form of shear-baroclinic instability (dashed line with stars). When $F_h \geq 0.4$, baroclinic instability for $m = 2$ (dashed line with crosses) becomes quickly strongly unstable as F_h increases (with a growth rate higher than the upper limit of figure 18a) but with a constant frequency $\omega_r \simeq 0.5\Omega_0$. Examples of modes corresponding to these three types of instability for $m = 2$ are shown in figure 20. For small F_h , shear instability (figure 20a) is strongly localized near $z = 0$ where the radial shear is maximum. In contrast, baroclinic-shear instability (figure 20b,c) occupies the whole pancake vortex as already seen in section 3.3.

4.3 Effect of the aspect ratio

We now vary the aspect ratio keeping the other parameters to the same values as before: $F_h = 0.3, Ro = 1.25$ and $Re = 10000$ (figure 21). For $m = 1$, the displacement mode (dotted line with squares) remains only marginally unstable while the growth rate of Gent-McWilliams instability (dashed line with triangles) is large but varies non-monotonically with the aspect ratio. It exhibits two maxima, for $\alpha \simeq 1$ and for large α . For very small α , the growth rate rises again but the instability is then under the form of the mixed baroclinic-Gent-McWilliams instability. The full spectra for three aspect ratios are displayed in figure 22 along with the spectra for $\alpha = \infty$, i.e. for a columnar vortex (solid line). For small aspect ratio (figure 22a), there exist only two unstable modes: the displacement mode near the origin and baroclinic-Gent-McWilliams instability near $\omega = 0.2\Omega_0$ whose eigenmode is shown in figure 23a. This markedly differs from the columnar case (solid line). In contrast, for larger aspect ratios ($\alpha = 3$, figure 22b), many modes are present within the frequency range of the columnar vortex. They are however less unstable than for $\alpha = 0.38$. At even larger aspect ratio $\alpha = 10$ (figure 22c), the spectrum becomes denser with a bell shape resembling the spectra of the columnar vortex. However, the maximum growth rate for the columnar vortex is still higher. The most unstable eigen-

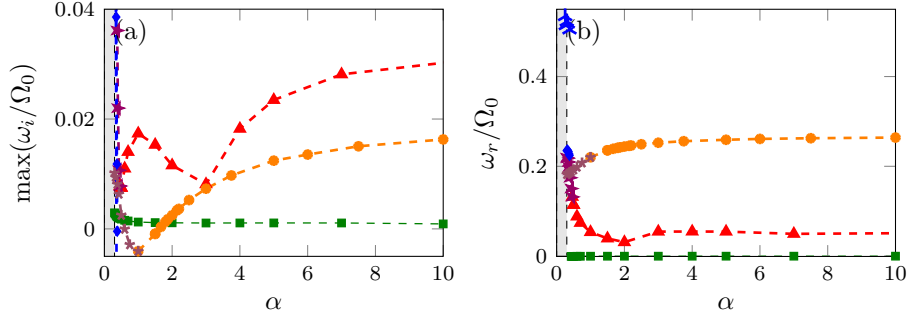


Figure 21: (Colour online) (a) Maximum growth rates and (b) corresponding frequencies as a function of aspect ratio α for $F_h = 0.3$, $Ro = 1.25$ and $Re = 10000$ of the different instabilities: displacement mode (\blacksquare); Gent-McWilliams instability (\blacktriangle); baroclinic-Gent-McWilliams instability (\star); baroclinic instability (\blacklozenge) for $m = 1$; shear instability (\bullet); baroclinic-shear instability (\star) and baroclinic instability for $m = 2$ (\blacktriangle). The shaded area indicates the gravitationally unstable region.

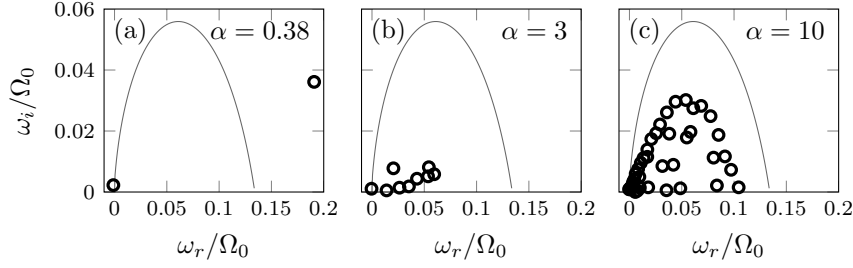


Figure 22: Growth rate (ω_i/Ω_0) and frequency (ω_r/Ω_0) spectra for $m = 1$ for different aspect ratios: (a) $\alpha = 0.38$, (b) $\alpha = 3$ and (c) $\alpha = 10$ for $F_h = 0.3$, $Ro = 1.25$, and $Re = 10000$. The solid line (—) indicates the spectrum for the columnar vortex for the same F_h , Ro and Re .

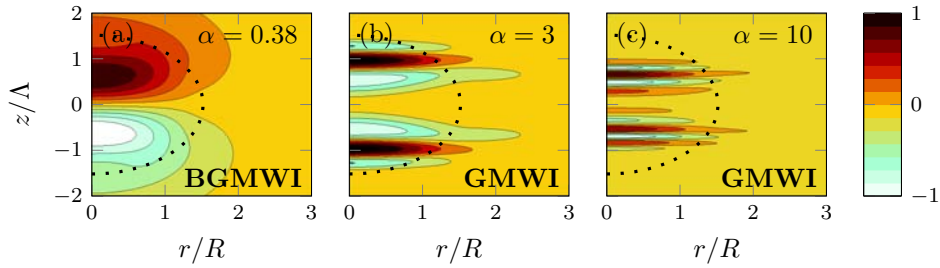


Figure 23: (Colour online) Real part of the radial velocity perturbation $\text{Re}(u_r)$ of the most unstable mode for different aspect ratios: mixed baroclinic-Gent-McWilliams instability (a) $\alpha = 0.38$ and Gent-McWilliams instability for (b) $\alpha = 3$ and (c) $\alpha = 10$ for $F_h = 0.3$, $Ro = 1.25$ and $Re = 10000$. The dotted line indicates the extension of the base flow by showing the contour where $\Omega = 0.1\Omega_0$.

mode for $\alpha = 10$ (figure 23c) presents a vertical wavelength $\lambda \simeq 5.23R$ close to the most amplified wavelength of the columnar vortex $\lambda \simeq 4.5R$. A longer typical wavelength $\lambda \simeq 6.16R$ is observed for $\alpha = 3$ (figure 23b).

As seen in figure 21a, shear instability (dashed line with filled circles) is only unstable for large aspect ratio $\alpha \geq 2$. However, for small α , it reappears in the form of the mixed baroclinic-shear instability (dashed line with stars). The pure baroclinic instability for $m = 2$ (dashed line with cross) also arises for very small aspect ratio.

4.4 Scaling in terms of the vertical Froude number

The two previous sections have revealed different growth rate variations as a function of the Froude number F_h and aspect ratio α . However, figure 24 shows that these growth rate variations are actually almost identical when represented as a function of the vertical Froude number F_h/α . The only deviation from this self-similarity is for small F_h/α : when $F_h/\alpha < 0.1$, the growth rate of Gent-McWilliams instability grows with decreasing F_h/α when α is varied and F_h kept constant whereas it decreases when α is fixed and F_h is varied. A small discrepancy is also observed for $m = 2$ when F_h/α is small. These differences come from viscous effects due to vertical shear since they scale like $1/\mathcal{R}$ where $\mathcal{R} = ReF_h^2$ is the buoyancy Reynolds number, because the typical vertical scale L_v scales like $L_v \sim F_h R$. Thus, viscous effects increase when the Froude number decreases keeping the Reynolds number constant. To prove this, the results for a smaller Froude number $F_h = 0.05$ but higher Reynolds number $Re = 360000$ are also displayed in figure 24 (black filled symbols). This Reynolds number has been chosen so that the buoyancy Reynolds number $\mathcal{R} = 900$ is the same as for $F_h = 0.3$ and $Re = 10000$. We see that the growth rate variations are almost identical for these two parameter sets confirming that the vertical Froude number scaling holds if the buoyancy Reynolds number is sufficiently large.

If the Rossby number is also varied but kept small, the growth rate curves for different Ro collapse when represented as a function of $2F_h/(\alpha Ro) = 1/\sqrt{Bu}$ in agreement with the quasi-geostrophic theory (figure 25). We can notice that the transition from Gent-McWilliams instability to baroclinic-Gent-McWilliams instability occurs near $Bu \simeq 1$ like in figure 24a (see the upper x axis) and in quasi-geostrophic fluid (Nguyen *et al.*, 2012). However, the growth rate curves are no longer self-similar when $2F_h/(\alpha Ro)$ approaches the threshold (15) for gravitational instability. Indeed, this threshold depends on Ro and is thus different for $Ro = 0.2$ and $Ro = 0.5$. The transition from shear instability to baroclinic-shear instability also occurs around $Bu = 1$ (figure 25b).

5 Energy budget

The previous section has evidenced a transformation of both shear and Gent-McWilliams instabilities into mixed baroclinic instabilities when the vertical Froude number is above a threshold. This transformation is apparent from the frequency and the structure of the modes. In order to confirm these transformations from the point of view of the energetics, we have computed the energy budget of the modes. To do so, the linearized equations (8) – (11) have been multiplied by the complex conjugate $(u_r^*, u_\theta^*, u_z^*, \rho^*)$, respectively, and their real

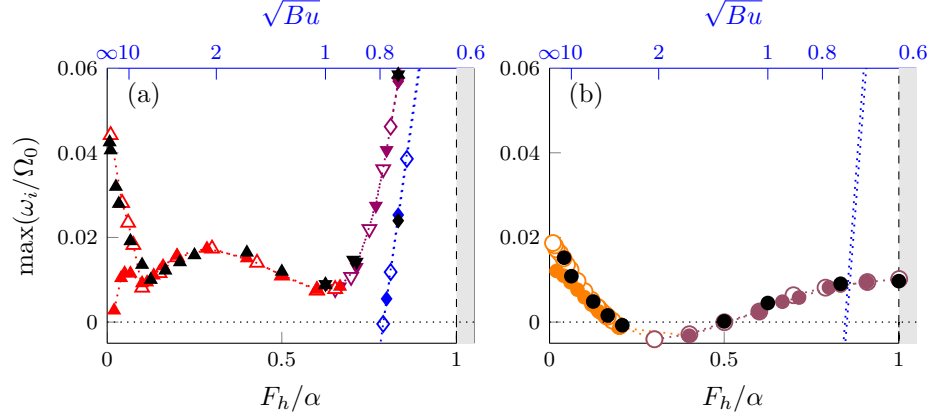


Figure 24: (Colour online) Maximum growth rates as a function of vertical Froude number F_h/α for $Ro = 1.25$, $Re = 10000$, (a) $m = 1$ and (b) $m = 2$. The upper x axis indicates the corresponding value of \sqrt{Bu} . The filled colored symbols shows the results when F_h is varied for $\alpha = 0.5$, open symbols when α is varied for $F_h = 0.3$, $Re = 10000$ and black filled symbols when α is varied for $F_h = 0.05$ and $Re = 360000$. The shaded area indicates the gravitationally unstable region. Different symbols are used for each instability: Gent-McWilliams ($\cdot\cdot\Delta\cdot\cdot$), baroclinic-Gent-McWilliams ($\cdot\cdot\nabla\cdot\cdot$), shear ($\cdot\cdot\bigcirc\cdot\cdot$), baroclinic-shear ($\cdot\cdot\bigcirc\cdot\cdot$) and baroclinic ($\cdot\cdot\Diamond\cdot\cdot$) instabilities.

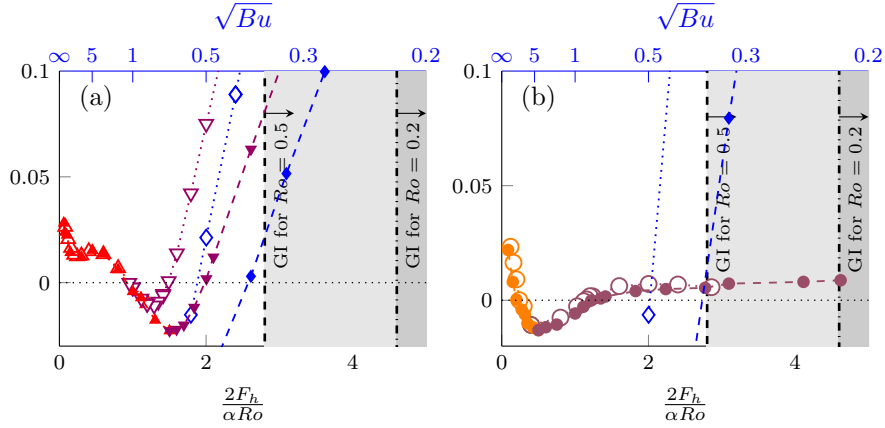


Figure 25: (Colour online) Maximum growth rates as a function of $2F_h/(\alpha Ro)$ for $Ro = 0.5$ (open symbols) and $Ro = 0.2$ (filled symbols) for $F_h = 0.3$, $Re = 10000$ (a) $m = 1$ and (b) $m = 2$. The upper x axis indicates the corresponding value of \sqrt{Bu} . Different symbols are used for each instability: Gent-McWilliams ($\cdot\cdot\Delta\cdot\cdot$), baroclinic-Gent-McWilliams ($\cdot\cdot\nabla\cdot\cdot$), shear ($\cdot\cdot\bigcirc\cdot\cdot$), baroclinic-shear ($\cdot\cdot\bigcirc\cdot\cdot$) and baroclinic ($\cdot\cdot\Diamond\cdot\cdot$) instabilities. The vertical dashed and dashed-dotted lines show the thresholds for gravitational instability for $Ro = 0.5$ and $Ro = 0.2$, respectively.

part have been integrated over the flow domain. This gives the energy balances:

$$\omega_i E_k - S_k = -B - D_k, \quad (23)$$

$$\omega_i E_p - S_p = B - D_p, \quad (24)$$

where

$$E_k = \int_{-Z_{\max}}^{Z_{\max}} \int_0^{R_{\max}} \frac{1}{2} (u_r u_r^* + u_\theta u_\theta^* + u_z u_z^*) r dr dz, \quad (25)$$

$$E_p = \int_{-Z_{\max}}^{Z_{\max}} \int_0^{R_{\max}} \frac{\rho \rho^*}{2N^2} r dr dz, \quad (26)$$

$$S_k = -\frac{1}{4} \int_{-Z_{\max}}^{Z_{\max}} \int_0^{R_{\max}} r \frac{\partial \Omega}{\partial r} (u_r^* u_\theta + u_\theta^* u_r) + r \frac{\partial \Omega}{\partial z} (u_z^* u_\theta + u_z u_\theta^*) dr dz, \quad (27)$$

$$S_p = -\frac{1}{4} \int_{-Z_{\max}}^{Z_{\max}} \int_0^{R_{\max}} \left(\frac{g}{\rho_0 N^2} \frac{\partial \rho_b}{\partial r} (u_r^* \rho + \rho^* u_r) + \frac{g}{\rho_0 N^2} \frac{\partial \rho_b}{\partial z} (u_z^* \rho + \rho^* u_z) \right) r dr dz, \quad (28)$$

$$B = \frac{1}{4} \int_{-Z_{\max}}^{Z_{\max}} \int_0^{R_{\max}} (\rho u_z^* + \rho^* u_z) r dr dz. \quad (29)$$

E_k and E_p are the kinetic and potential energies of the perturbation. The term S_k (S_p) represents the transfer of kinetic (potential) energy from the base flow to the perturbation. The term B is the energy conversion from the kinetic to potential energy of the perturbation. D_k and D_p are the kinetic and potential energy dissipations. They are small and will not be discussed here. The transfers are plotted in figure 26 as a function of F_h/α for $m = 1$ (figure 26a) and $m = 2$ (figure 26b) for $Ro = 1.25$ and $Re = 10000$. These parameters correspond to the colored filled/open symbols in figure 24. For both $m = 1$ and $m = 2$, the kinetic energy transfer S_k is positive for $F_h/\alpha < 0.5$ (corresponding to $Bu > 1.5$), while the potential energy transfer S_p is smaller and negative. This means that the source of the instability is the kinetic energy of the base flow like for the instabilities of a columnar vortex ($\alpha = \infty$). A part of the kinetic energy of the perturbation is converted to potential energy since the energy conversion B is positive except for $m = 2$ for $F_h/\alpha < 0.1$ when $F_h > 0.5$ (figure 26b). In contrast, when $F_h/\alpha > 0.5$ ($Bu < 1.5$), the potential energy transfer S_p becomes positive while S_k is negative. The energy source of the instability is therefore the potential energy of the base flow.

Figure 27 shows that a similar transition occurs when Ro is varied while F_h and α are kept constants. The transfers for $m = 1$ (figure 27a) correspond to those of Gent-McWilliams and baroclinic Gent-McWilliams instabilities shown in figure 10. As Ro decreases, the source of the energy perturbation changes from kinetic to potential around $Ro \simeq 2 - 3$ when Gent-McWilliams instability transforms into the mixed baroclinic Gent-McWilliams instability. The same happens for $m = 2$ (figure 27b) around $Ro \simeq 1$ when shear instability changes

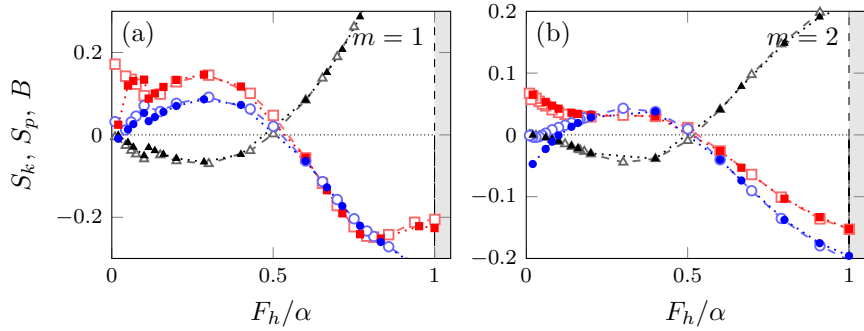


Figure 26: (Colour online) Kinetic and potential energy transfers S_k ($\cdots\blacksquare\cdots$), S_p ($\cdots\bullet\cdots$) and energy conversion B ($\cdots\blacktriangle\cdots$) as a function of the vertical Froude number F_h/α for (a) $m = 1$ and (b) $m = 2$ for $Ro = 1.25$ and $Re = 10000$. The filled symbols indicate when F_h is varied for $\alpha = 0.5$ and open symbols when α is varied for $F_h = 0.3$.

into baroclinic-shear instability (see figure 15). This confirms that the baroclinicity plays an important role for large F_h/α or small Ro and the instabilities are then of mixed nature: baroclinic-Gent-McWilliams and baroclinic-shear instabilities.

6 Condition of existence of shear instability

In this section, we will show that the variations of the growth rate of shear instability for $m = 2$ as a function of Ro , F_h and α can be directly understood from the characteristics of the shear instability for a columnar vortex. As demonstrated in part 1 for stratified non-rotating fluids, the shear instability for columnar vortices only exists for vertical wavenumbers k in the range $kRF_h < 1.6$. The minimum vertical wavelength is therefore $\lambda_{\min} \simeq 4F_hR$. One wavelength will fit in the thickness of the pancake vortex $2\alpha R$ only if $F_h/\alpha < 0.5$. This condition turns out to explain very well the existence of shear instability for pancake vortices in stratified non-rotating fluids. Here, we extend this criterion to arbitrary Rossby number Ro .

Figure 28a shows the growth rate of shear instability for a columnar vortex as a function of the rescaled vertical wavenumber kRF_h . The growth rate is maximum in the 2D limit $k = 0$ and decreases monotonically as kRF_h increases. When F_h is varied between 0.1 and 2 with Ro fixed, all the curves remain similar and stabilize for $kRF_h \simeq 0.6$. This illustrates the fact that the growth rate depends only on kRF_h for small F_h for any given Ro . The growth rate of shear instability is shown in figure 28b as a function of Ro and kRF_h . The wavenumber cutoff kRF_h first increases as Ro decreases from $Ro = \infty$ and then decreases and follows the quasi-geostrophic scaling law $kRF_h/Ro = \text{const}$ for small Rossby numbers. For negative Rossby numbers, the cutoff re-increases monotonically as Ro decreases. This shows that the wavenumber cutoff can be written $kF_hR = c(Ro)$, where c is a function of Ro . A similar evolution of the cutoff of shear instability is observed for parallel horizontal flows sheared horizontally in strongly stratified rotating fluids. In particular, in the case of

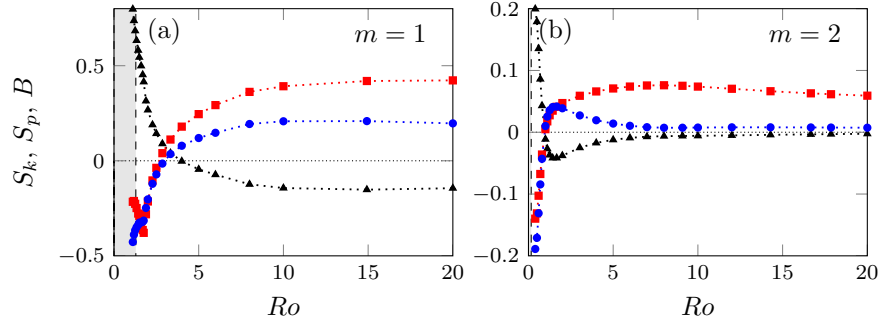


Figure 27: (Colour online) Kinetic and potential energy transfers S_k ($\cdots\blacksquare\cdots$) and S_p ($\cdots\blacktriangle\cdots$) and energy conversion B ($\cdots\bullet\cdots$) as a function of the Rossby number Ro for (a) $m = 1$, $\alpha = 0.5$ and for (b) $m = 2$, $\alpha = 1.2$ for $F_h = 0.5$ and $Re = 10000$. The plot (a) corresponds to Gent-McWilliams, baroclinic Gent-McWilliams and baroclinic instabilities shown in figure 10. The plot (b) corresponds to shear and baroclinic shear instabilities shown in figure 15.

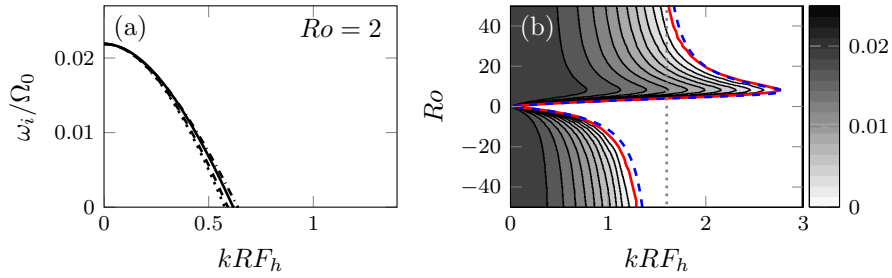


Figure 28: (Colour online) Growth rate of shear instability for $m = 2$ for a columnar vortex as a function of the rescaled axial wavenumber kRF_h : (a) for different Froude numbers F_h : \cdots $F_h = 0.1$; — $F_h = 0.5$; $---$ $F_h = 1$; $-\cdot-\cdot-$ $F_h = 2$, for $Ro = 2$ and $Re = 10000$. (b) Growth rate ω_i/Ω_0 contours of shear instability for a columnar vortex as a function of the Rossby number Ro and the rescaled vertical wavenumber kRF_h for $F_h = 0.2$ and $Re = 10000$. The vertical dotted line is the wavenumber cutoff $kRF_h = 1.6$ for $Ro = \infty$.

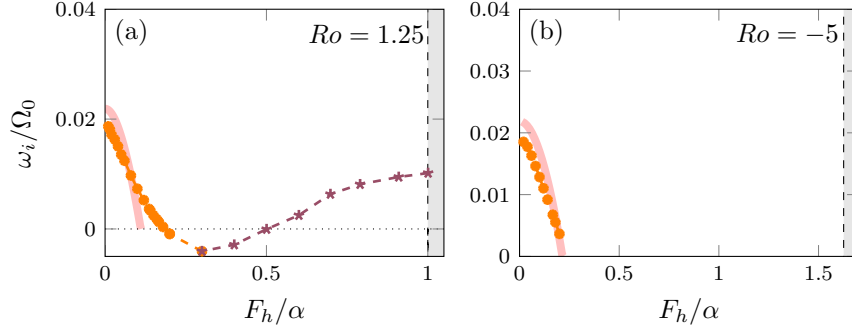


Figure 29: (Colour online) Maximum growth rate of shear instability for columnar (for $kR = \pi/\alpha$) (—) and pancake (—•—) vortices as a function of F_h/α for $m = 2$, $F_h = 0.3$ and $Re = 10000$ for (a) $Ro = 1.25$ and (b) $Ro = -5$. The shaded region is the gravitationally unstable region. The line —*— in (a) indicates the growth rate of baroclinic-shear instability.

the hyperbolic tangent (\tanh) profile, Blumen (1971) has obtained an analytical expression for the neutral wavenumbers: $(F_h k_z)^2(1 - 1/Ro)^2 + k_x^2 = 1$, where k_x and k_z are the streamwise and vertical (spanwise) wavenumbers, respectively. In the present case, we did not find an exact expression for the cutoff vertical wavenumber but, guided by the expression of Blumen (1971), we have found that $c(Ro)$ can be well approximated by

$$c(Ro) = \frac{1}{\sqrt{c_1 + \frac{c_2}{Ro} + \frac{c_3}{Ro^2}}}, \quad (30)$$

where $c_1 = 0.44$, $c_2 = -4.8$ and $c_3 = 18.2$ are empirical constants. The rescaled cutoff vertical wavenumber kRF_h obtained from (30) is shown by a dashed line in figure 28b. The minimum vertical wavelength of shear instability for a columnar vortex in a strongly stratified fluid for an arbitrary Rossby number is therefore $\lambda_{\min} = 2\pi F_h R/c(Ro)$. Hence, one wavelength will fit within the thickness of the pancake vortex if $\lambda_{\min} \leq 2\alpha R$, i.e. if $F_h/\alpha \leq c(Ro)/\pi$.

Assuming further that the equivalent vertical wavenumber of the most unstable mode of shear instability for the pancake vortex is always the smallest fitting along the vertical, i.e. $kR = \pi/\alpha$, one can compare the growth rate of shear instability for columnar and pancake vortices as done in figure 29 for two different Rossby numbers $Ro = 1.25$ and $Ro = -5$. For both Ro , the growth rate for columnar and pancake vortices are in good agreement and vanish around the same value of F_h/α (or equivalently kRF_h/π). For $Ro = 1.25$, the growth rate for the pancake vortex rises again for $F_h/\alpha > 0.5$ owing to the mixed baroclinic-shear instability.

A similar comparison is made in figure 30 but now as a function of the Rossby number for the parameters $\alpha = 1.2$, $F_h = 0.5$ and $Re = 10000$ that have been presented in section 3.3. The maximum growth rate of shear instability for the pancake vortex agrees quite well with the one of the columnar vortex for the vertical wavenumber $kR = \pi/\alpha$. In particular, shear instability is stabilized in the same range of Rossby number: $-22 \lesssim Ro \lesssim 3$. Again, the growth rate for the pancake vortex rises for small Rossby number but under the mixed form

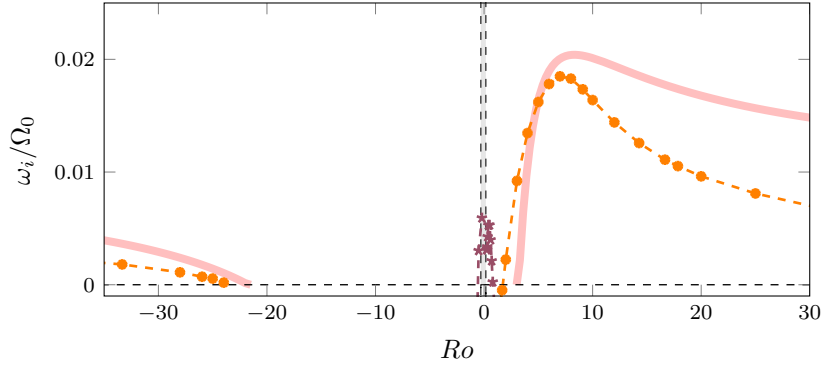


Figure 30: (Colour online) Maximum growth rate of shear instability for columnar (for $kR = \pi/\alpha$) (—) and pancake ($\alpha = 1.2$) (-●-) vortices as a function of Ro for $m = 2$, $F_h = 0.5$ and $Re = 10000$. The shaded region is the gravitationally unstable region. The line -*- indicates the growth rate of baroclinic-shear instability.

of baroclinic-shear instability.

As a conclusion, these results demonstrate that the maximum growth rate of shear instability in pancake vortices corresponds in good approximation to its growth rate in columnar vortices for the smallest vertical wavenumber $kR = \pi/\alpha$ fitting in the pancake vortex. When this wavenumber is beyond the upper wavenumber cutoff, i.e. $\pi/\alpha > c(Ro)/F_h$, shear instability is suppressed in pancake vortices.

7 Scaling laws for Gent-McWilliams instability

The fluctuations of the growth rate of Gent-McWilliams instability as a function of the vertical Froude number F_h/α (figure 24a) can be also understood by comparison to the columnar case. First, the equivalent vertical wavenumber k of Gent-McWilliams instability for pancake vortices can be estimated as $k = 2\pi/\lambda$ where λ is twice the vertical distance between contiguous minimum and maximum of the radial velocity perturbation. The growth rate is plotted as a function of this wavenumber scaled by $F_h R$ in figure 31 (symbols). The corresponding growth rate for a columnar vortex is shown by the grey continuous line.

Let us first focus on figure 31a where the Froude number is fixed to $F_h = 0.3$ while the aspect ratio varies. When α increases from $\alpha = 0.5$ to $\alpha = 3$, the growth rate of Gent-McWilliams instability for the pancake vortex (dotted line with triangles) increases and then decreases in a similar fashion as the columnar case. In particular, the growth rate is maximum for $kRF_h = 0.6$ near the most amplified wavenumber kRF_h of the columnar vortex. Nevertheless, the growth rate maximum for the pancake vortex is much smaller than for the columnar vortex. Along the curve, the eigenmodes remain similar to the one shown in figure 19b, i.e. the mode has a single oscillation along the vertical and occupies the whole pancake vortex. However, when $\alpha = 3$, a secondary mode with several oscillations along the vertical (see figure 23b) starts to have a growth rate as high

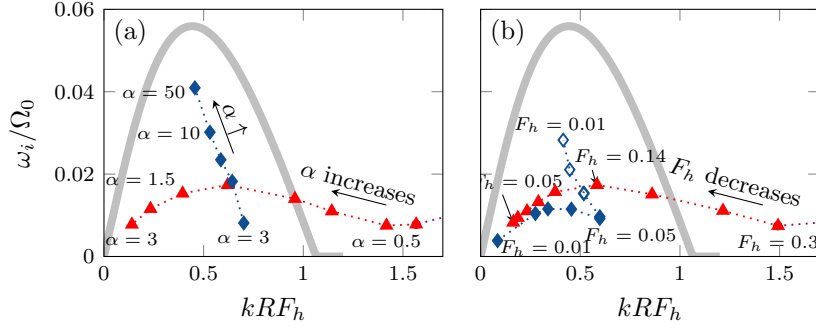


Figure 31: (Colour online) Maximum growth rate of Gent-McWilliams instability ($m = 1$) as a function of the estimated vertical wavenumber kRF_h for $Ro = 1.25$ and $Re = 10000$. (a) α is varied for $F_h = 0.3$ and (b) F_h is varied for $\alpha = 0.5$. The thick grey line corresponds to the growth rate of the columnar vortex for the same parameters. Two different symbols are used depending on F_h/α : $\cdots\blacktriangle\cdots$ for $F_h/\alpha > 0.1$ and $\cdots\blacklozenge\cdots$ for $F_h/\alpha < 0.1$. Open diamond symbols ($\cdots\blacklozenge\cdots$) in (b) indicate the growth rates when the buoyancy Reynolds number is kept constant $\mathcal{R} = F_h^2 Re = 25$ when F_h is varied for $\alpha = 0.5$.

as the primary mode. The wavenumber of this secondary mode is much higher and its growth rate is shown by the dashed line with diamonds in figure 31a. When α is further increased, the growth rate of this secondary mode increases rapidly but its estimated wavenumber decreases only slightly toward the most amplified wavenumber of the columnar vortex. Along this curve, the eigenmode has therefore more and more oscillations along the vertical like in figure 23c. In other words, the confinement effect due to the pancake shape becomes weaker as the vortex becomes taller.

Alternatively, when α is kept constant to $\alpha = 0.5$ (figure 31b), a similar evolution is first observed when the Froude number is decreased from $F_h = 0.3$ to $F_h = 0.05$ (dashed line with triangles). When $F_h = 0.05$, a secondary mode (dashed line with diamonds) becomes as unstable as the primary mode. This occurs for the same vertical Froude number $F_h/\alpha = 0.1$ as in figure 31a. The structure of this secondary mode can be seen in figure 19a. However, the growth rate of the secondary mode first increases slightly as F_h is further decreased and then it decreases toward zero while its wavenumber also decreases. The difference in behaviour compared to figure 31a comes from the fact that the buoyancy Reynolds number $\mathcal{R} = ReF_h^2$ becomes too low when the Froude number F_h is decreased below 0.05. Indeed, if the Reynolds number is increased at the same time as F_h is decreased so as to keep the buoyancy Reynolds number constant $\mathcal{R} = 25$, the growth rate (open diamonds in figure 31b) rises toward the growth rate peak for the columnar vortex as F_h decreases like in figure 31a.

8 Detailed study of baroclinic instability

In sections 3 and 4, baroclinic instability has been observed for $m = 1$ and $m = 2$ near the threshold for gravitational instability. Here, we will further study its dependence on the Rossby number Ro and the vertical Froude number

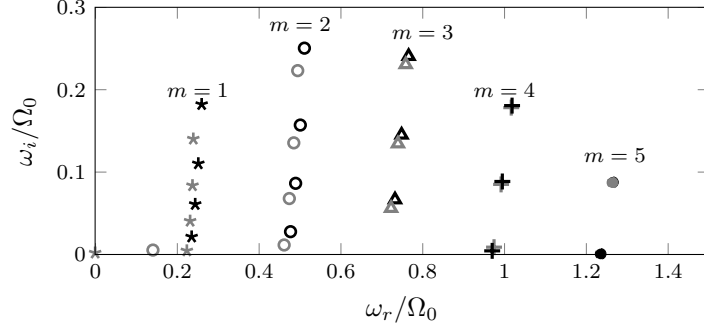


Figure 32: Growth rate (ω_i/Ω_0) and frequency (ω_r/Ω_0) spectra for different azimuthal wavenumbers: $m = 1$ (\star); $m = 2$ (\circ); $m = 3$ (\blacktriangle); $m = 4$ (\blackplus); $m = 5$ (\bullet) for $\alpha = 0.5$, $F_h = 0.3$, $Ro = 0.4$, and $Re = 10000$. Grey and black symbols indicate symmetric and anti-symmetric modes, respectively.

F_h/α . In addition, we will show that baroclinic instability destabilizes also higher azimuthal wavenumbers. A theoretical criterion and scaling laws for baroclinic instability will be next derived following the approach used in part 1 for stratified non-rotating fluids.

8.1 A typical example

Figure 32 shows the spectra for $\alpha = 0.5$, $F_h = 0.3$, $Ro = 0.4$ and $Re = 10000$ for different azimuthal wavenumbers m . These control parameters are just below the threshold of gravitational instability which is $F_h = 0.32$ for $\alpha = 0.5$ and $Ro = 0.4$. Among all azimuthal wavenumbers, $m = 2$ is the most unstable. For each m , the most unstable mode is anti-symmetric (black symbol) and the second most unstable mode is symmetric (grey symbol). Nevertheless, the growth rate difference between anti-symmetric and symmetric modes becomes very small as m increases. We will show that these modes are due to baroclinic instability. However, the displacement mode is also observed for $m = 1$ near the origin and baroclinic-shear instability for $m = 2$ is located near $\omega_r/\Omega_0 = 0.18$ with a small growth rate. Note also that the leading mode for $m = 1$ is baroclinic-Gent-McWilliams instability which derives continuously from Gent-McWilliams instability. For higher azimuthal wavenumbers $m \geq 3$, only baroclinic instability exists. No instability has been found for $m = 0$ and $m \geq 6$. The characteristic frequency of each azimuthal wavenumber is proportional to m : $\omega_r/\Omega_0 \simeq 0.25m$, i.e. the azimuthal phase velocity is constant. In fact, this corresponds to the angular velocity of the base flow $\Omega(r_b, z_b) \simeq 0.25$ at the point $r_b = 0$, $z_b = 1.17\Lambda$ where the vertical density gradient $\partial\rho_t/\partial z$ is maximum for $\alpha = 0.5$, $F_h = 0.3$ and $Ro = 0.4$.

Figure 33 shows the first three anti-symmetric eigenmodes for $m = 3$. As already shown for $m = 1$ (figure 9), the number of oscillations in the radial direction increases with the mode number while the vertical structure remains the same. Figure 34a shows the growth rate as a function of the radial wavenumber $l = 2\pi/\lambda_r$, where the radial wavelength λ_r is estimated as twice the distance between two successive extrema as illustrated in figure 33b. For each azimuthal

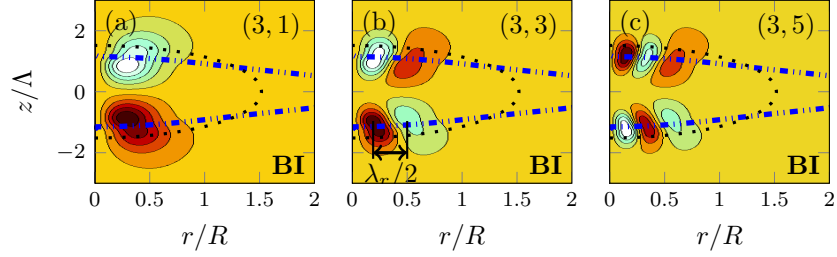


Figure 33: (Colour online) Real part of the radial velocity perturbation $\text{Re}(u_r)$ for the first three anti-symmetric baroclinic eigenmodes for $m = 3$: (a) $(3, 1)$, (b) $(3, 3)$ and (c) $(3, 5)$ for $\alpha = 0.5$, $F_h = 0.3$, $Ro = 0.4$ and $Re = 10000$. The dotted line indicates the extension of the base flow by showing the contour where $\Omega = 0.1\Omega_0$. The double dotted dashed line ($\blacksquare \cdots \blacksquare$) shows where the isopycnal potential vorticity gradient (22) changes sign.

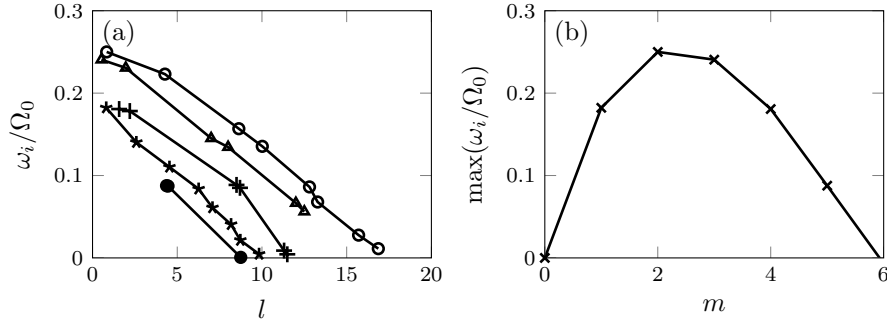


Figure 34: (a) Growth rate (ω_i/Ω_0) as a function of the radial wavenumber l for different azimuthal wavenumbers: $m = 1$ (\star); $m = 2$ (\odot); $m = 3$ (\blacktriangle); $m = 4$ (\oplus); $m = 5$ (\bullet) and (b) maximum growth rate as a function of the azimuthal wavenumber m for $\alpha = 0.5$, $F_h = 0.3$, $Ro = 0.4$, and $Re = 10000$.

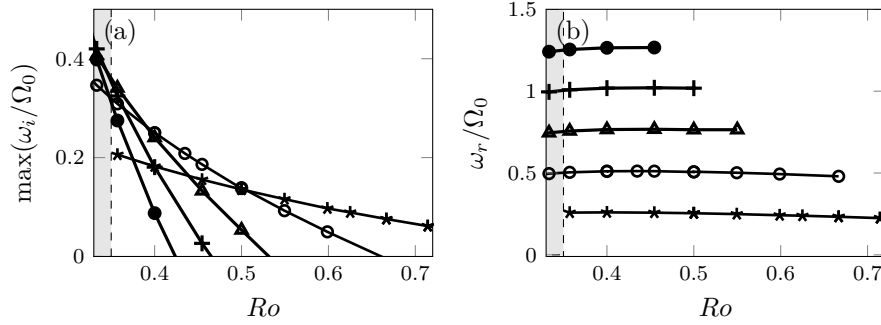


Figure 35: (a) Maximum growth rate and (b) corresponding frequency of baroclinic instability (dark solid lines) as a function of Ro for different azimuthal wavenumbers: $m = 1$ (\star); $m = 2$ (\circ); $m = 3$ (\blacktriangle); $m = 4$ ($+$); $m = 5$ (\bullet) for $\alpha = 0.5, F_h = 0.3$ and $Re = 10000$. The shaded area indicates the gravitationally unstable region.

wavenumber, the growth rate decreases monotonically as l increases. As already visible in figure 32, the maximum growth rate exhibits a bell-shape curve as a function of m (figure 34b). These wavenumber properties are very reminiscent of baroclinic instability in parallel shear flows (Vallis, 2006).

8.2 Parametric study

Figure 35 outlines the effect of the Rossby number on the maximum growth rate and corresponding frequency of the baroclinic instability for each azimuthal wavenumber for $\alpha = 0.5, F_h = 0.3$ and $Re = 10000$. When Ro increases, the growth rate decreases faster as m increases. Hence, $m = 3$ is the most unstable azimuthal wavenumber when Ro is close to the threshold for the gravitational instability whereas $m = 1$ becomes the most unstable for $Ro \geq 0.5$. In between, $m = 2$ is the most unstable. In contrast, the frequency of each azimuthal wavenumber is independent of the Rossby number (figure 35b). Similarly, figure 36 shows the effect of the Froude number for $\alpha = 0.5, Ro = 0.4$ and $Re = 10000$. The frequency is again independent of the Froude number (figure 36b) whereas the maximum growth rate (figure 36a) increases with F_h/α at a rate increasing with m .

8.3 A simple analytical model

In part 1, a model consisting of a bounded vortex with an angular velocity varying only in the vertical direction has been considered and shown to account qualitatively for the characteristics of baroclinic instability in stratified non-rotating fluids. Such a model takes into account the main features of the base flow in the core of the pancake vortex where baroclinic instability develops. Its stability can be solved analytically when the vertical variations are weak. Here, this model is extended to take into account a background rotation. The base angular velocity of the vortex is assumed to be

$$\Omega = \tilde{\Omega}_0 - \tilde{\Omega}_1 z, \quad (31)$$

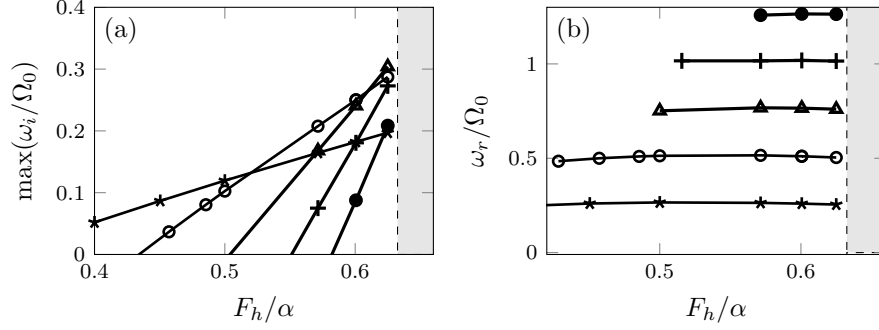


Figure 36: (a) Maximum growth rate and (b) corresponding frequency of baroclinic instability (dark solid lines) as a function of F_h/α for different azimuthal wavenumbers: $m = 1$ (\star); $m = 2$ (\circ); $m = 3$ (\blacktriangle); $m = 4$ (\blackplus); $m = 5$ (\bullet) for $\alpha = 0.5$, $Ro = 0.4$, and $Re = 10000$. The shaded area indicates the gravitationally unstable region.

where $\tilde{\Omega}_0$ and $\tilde{\Omega}_1$ are constants. From the thermal-wind relation (4), the base density is obtained as

$$\rho_b = \frac{\rho_0}{g} \left[\tilde{\Omega}_0 + \frac{f}{2} - \tilde{\Omega}_1 z \right] \tilde{\Omega}_1 r^2. \quad (32)$$

As in part 1, we consider that the base flow is contained in a rigid cylinder of radius R and height H between $z = -H/2$ and $z = H/2$. By assuming that the vertical variations are weak, i.e. $\tilde{\Omega}_1 H \ll |\tilde{\Omega}_0 + f/2|$, the equation (8)–(12) in the inviscid limit can be reduced at leading order in $\tilde{\Omega}_1$ to

$$\frac{1}{r} \frac{\partial}{\partial r} \left(r \frac{\partial p}{\partial r} \right) - \left[\frac{m^2}{r^2} + C^2 \frac{\partial^2}{\partial z^2} \right] p = 0 + O(\tilde{\Omega}_1^2), \quad (33)$$

where $C = 2|\tilde{\Omega}_0 + f/2|/N$. Note that the hypothesis $\tilde{\Omega}_1 H \ll |\tilde{\Omega}_0 + f/2|$ is not valid around $\tilde{Ro} \equiv 2\tilde{\Omega}_0/f = -1$. Here, the dimensionless numbers are denoted with tilde in order to distinguish them from the ones defined in (13). The Coriolis parameter f enters the problem only through the constant C in (33). The general solution of (33) is

$$p = J_m(Ckr) (A \cosh kz + B \sinh kz), \quad (34)$$

where J_m is the Bessel function of order m of the first kind and A and B are constants. Imposing the boundary conditions $u_z(z = \pm H/2) = 0$ and $u_r(r = R) = 0$ yields two relations similar to those for the classical Eady problem (Vallis, 2006)

$$\omega = m\tilde{\Omega}_0 + \frac{m\tilde{\Omega}_1}{k} \sqrt{\left(1 - \frac{kH}{2 \tanh(kH/2)}\right) \left(1 - \frac{kH \tanh(kH/2)}{2}\right)}, \quad (35)$$

$$CkR = \mu_{m,n}, \quad (36)$$

where $\mu_{m,n}$ is the n th root of J_m . Combining the condition for instability $kH < 2.4$ and the fact that $\mu_{m,n} > \mu_{1,1} = 3.83$, yield the instability condition

$$\frac{\tilde{F}_h}{\tilde{\alpha}} \left| 1 + \frac{1}{Ro} \right| > 0.8, \quad (37)$$

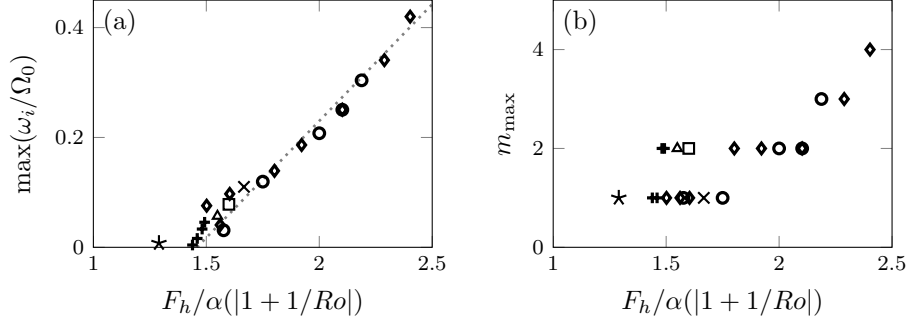


Figure 37: (a) Maximum growth rate and (b) most amplified azimuthal wavenumber m of baroclinic instability for different combinations of Ro and F_h : $Ro = 0.4$, F_h varies \circ , $F_h = 0.3$, Ro varies \diamond , $Ro = 1$, $F_h = 0.42$ \times , $Ro = 5$, $F_h = 0.67$ \square , $Ro = 10$, $F_h = 0.7$ \triangle , $Ro = -5$, $F_h = 0.8$ \star and $Ro = \infty$, F_h varies \clubsuit . Other parameters are fixed to $\alpha = 0.5$, $Re = 10000$. The dotted line in (a) is a fit.

where $\tilde{\alpha} = H/R$ and $\tilde{F}_h = \tilde{\Omega}_0/N$. This condition simply states that the Burger number $\tilde{B}u = \tilde{\alpha}^2 N^2 / (f + 2\tilde{\Omega}_0)^2$ based on the absolute angular velocity $\tilde{\Omega}_0 + f/2$ should be below a threshold $\tilde{B}u < 0.4$ for instability. When $\tilde{Ro} \ll 1$, (37) recovers the classical condition for baroclinic instability (Eady, 1949; Saunders, 1973; Hide & Mason, 1975). We can also derive scaling laws for the maximum growth rate and the most amplified wavenumber (35). For any m , the growth rate is maximum for the first root of the Bessel function $n = 1$. An asymptotic expansion of this root for large m is $\mu_{m,1} = m + 1.856m^{1/3} + O(m^{-1/3})$ (Abramowitz & Stegun, 1972). Taking only the leading order of this expansion, i.e. $\mu_{m,1} \sim m$, (36) implies $m/k = CR$. The growth rate is thus maximum when the term inside the square root in (35) is minimum, i.e. when $kH = 1.6$. The most amplified azimuthal wavenumber is therefore

$$m_{\max} \simeq 3.2 \frac{\tilde{F}_h}{\tilde{\alpha}} \left| 1 + \frac{1}{\tilde{Ro}} \right|, \quad (38)$$

and the maximum growth rate is

$$\omega_{i \max} \simeq 0.6 \tilde{\Omega}_1 R \frac{\tilde{F}_h}{\tilde{\alpha}} \left| 1 + \frac{1}{\tilde{Ro}} \right|, \quad (39)$$

for large m . These scaling laws are tested in figure 37 for baroclinic instability of the pancake vortex by assuming that $F_h/\alpha|1 + 1/Ro|$ is equivalent to $\tilde{F}_h/\tilde{\alpha}|1 + 1/Ro|$. Different combinations of F_h and Ro are shown for $\alpha = 0.5$ and $Re = 10000$. As seen in figure 37a, the maximum growth rates align along a straight line when represented as a function of $F_h/\alpha|1 + 1/Ro|$. Baroclinic instability only occurs for $F_h/\alpha|1 + 1/Ro| \geq 1.46$ in qualitative agreement with (37). Note that the leftmost point (star) in figure 37a, which is slightly away from the other points, is for a negative Rossby number $Ro = -5$. Similarly, figure 37b shows that the most amplified azimuthal wavenumber increases approximately linearly with $F_h/\alpha|1 + 1/Ro|$ in agreement with (38).

Figure 38 displays a map of the domain of existence of baroclinic instability in the parameter space $(F_h/\alpha, Ro)$. The dashed line represents the thresh-

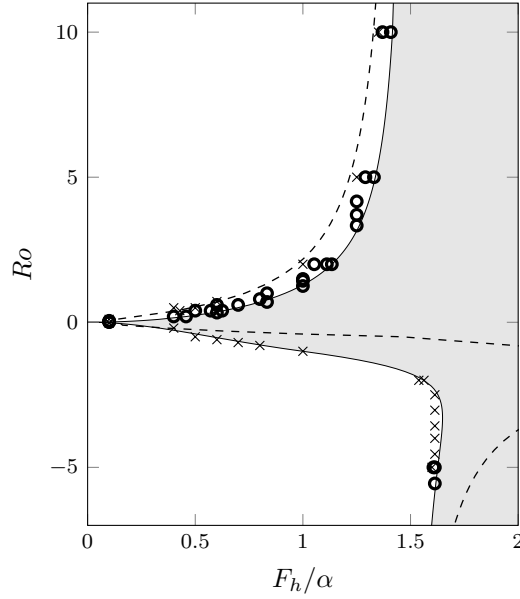


Figure 38: Domain of existence of baroclinic instability for $m = 2$ as a function of F_h/α and Ro for $\alpha = 0.5$ and $Re = 10000$: circles (o) indicate the parameters unstable to baroclinic instability, crosses (x) are for the stable case. The shaded area indicates the region unstable to gravitational instability and the dashed line (---) corresponds to the threshold $F_h/\alpha |1 + 1/Ro| = 1.46$.

old $F_h/\alpha |1 + 1/Ro| = 1.46$ deduced from figure 37a. The shaded region is gravitationally unstable. The circle symbols indicate the parameters for which baroclinic instability has been observed for $m = 2$, $Re = 10000$ and $\alpha = 0.5$ while the cross symbols correspond to the parameters stable to baroclinic instability for $m = 2$. We can see that there is a good agreement between the threshold $F_h/\alpha |1 + 1/Ro| = 1.46$ and the numerical results for positive Rossby number. However, the threshold departs from the numerical results for negative Rossby numbers around $Ro \simeq -5$. This is most likely due to the assumption of the slow vertical variation $\tilde{\Omega}_1 H \ll \tilde{\Omega}_0 + f/2$ used to derive the theoretical scaling laws. This hypothesis indeed breaks down around $\tilde{Ro} = -1$ and this may affect a large range of negative Rossby numbers Ro . Furthermore, the location where the density gradient is maximum actually varies with the Rossby number implying that Ω_0 also varies with Ro . These variations could be taken into account in a refined analysis.

9 Map of the instabilities

9.1 Parameter space $(F_h/\alpha, Ro)$

Figures 39a,c,e summarize the different instabilities observed for each azimuthal wavenumber $m = 0, 1$ and 2 in the parameter space $(F_h/\alpha, Ro)$ for $Re = 10000$ and various aspect ratios. The symbols indicate the instability type while the lines indicate the different semi-theoretical thresholds that have been derived

throughout the paper. These conditions are generally in good agreement with the numerical results for all the parameters investigated. In summary, centrifugal instability exists for $m = 0, 1, 2$ for sufficiently high Rossby and Froude numbers. The solid lines correspond to the thresholds for centrifugal instability for $\alpha = 0.5$ that can be obtained from the asymptotic formula (18). This formula shows that the aspect ratio of the vortex has no effect and there is a stabilization at low Froude numbers because the buoyancy Reynolds number $\mathcal{R} = ReF_h^2$, which controls viscous effects, decreases. Shear instability for $m = 2$ is present below a critical vertical Froude number F_h/α depending on the Rossby number $F_h/\alpha < c(Ro)/\pi$, where $c(Ro)$ is defined in (30) (dotted line in figure 39e). However, for higher F_h/α , it reappears under the mixed form of a baroclinic-shear instability when the Rossby number is not too large (dashed dotted line in figure 39e $Ro \lesssim 10F_h^2/\alpha^2$ for $Ro > 0$ and $Ro \gtrsim -1.1F_h/\alpha$ for $Ro < 0$). Gent-McWilliams instability for $m = 1$ (triangles in figure 39c) is observed over wide ranges of Ro and F_h/α except when it transforms to baroclinic-Gent-McWilliams (squares in figure 39c) for small Rossby numbers such that $F_h/\alpha > |Ro|/(2\sqrt{0.7Ro + 0.1})$ (dashed dotted lines in figure 39c). Baroclinic instability occurs when $F_h/\alpha|1 + 1/Ro| > 1.46$ (dashed lines in figure 39c,e), i.e. only in a small band close to the threshold for the gravitational instability (shaded region).

9.2 Parameter space (Bu , Ro)

Figures 39b,d,f display the same instability maps but focused on the region $|Ro| < 2$ which pertains to most mesoscale oceanic vortices. In addition, the x -axis is now the Burger number $Bu = Ro^2\alpha^2/(4F_h^2)$ instead of the vertical Froude number F_h/α . Indeed, the Burger number is more appropriate to describe the region of small Rossby number since it is the only non-dimensional parameter in the quasi-geostrophic limit. Only the range $0 \leq Bu \leq 2$ is displayed as in Nguyen *et al.* (2012). In these ranges, we see that centrifugal instability for $\alpha = 0.5$ exists only in the bottom left corner for sufficiently negative Ro and small Bu . Gent-McWilliams instability (triangles in figure 39d) occurs when $Bu \gtrsim 1$. In contrast, baroclinic-Gent-McWilliams instability exists mostly for positive Ro in a band adjacent to the domain of baroclinic instability. The threshold can be fitted approximately by $Bu \simeq 0.7Ro + 0.1$ (dashed dotted line in figure 39d). Hence, there is an intermediate range of Burger number where only the displacement mode is unstable for $m = 1$. For $m = 2$ (figure 39f), the domain of existence of baroclinic-shear instability is also contiguous to the domain unstable to baroclinic instability. The upper Burger number limit is given by $Bu \simeq 1.3/(-Ro + 2.26)$. Just above this threshold, $m = 2$ perturbations are stable since shear instability starts to be active only when $Bu \gtrsim 7$. These results are in general consistent with those in the quasi-geostrophic limit ($Ro \rightarrow 0$) in continuously stratified fluids (Nguyen *et al.*, 2012) or in two-layer fluids (Ikeda, 1981; Helfrich & Send, 1988; Flierl, 1988; Benilov, 2003). In particular, Flierl (1988) reports for piecewise profiles that the $m = 1$ mode is unstable for $Bu > 1$ while higher azimuthal modes, $m \geq 2$, are unstable to shear instability for $Bu > O(1)$ for sufficiently steep vorticity profiles and to baroclinic instability for $Bu < O(1)$ (see for example his figure 10b). A neutrally stable region around $Bu = O(1)$ is also observed for moderately steep vorticity profiles as in figure 39.

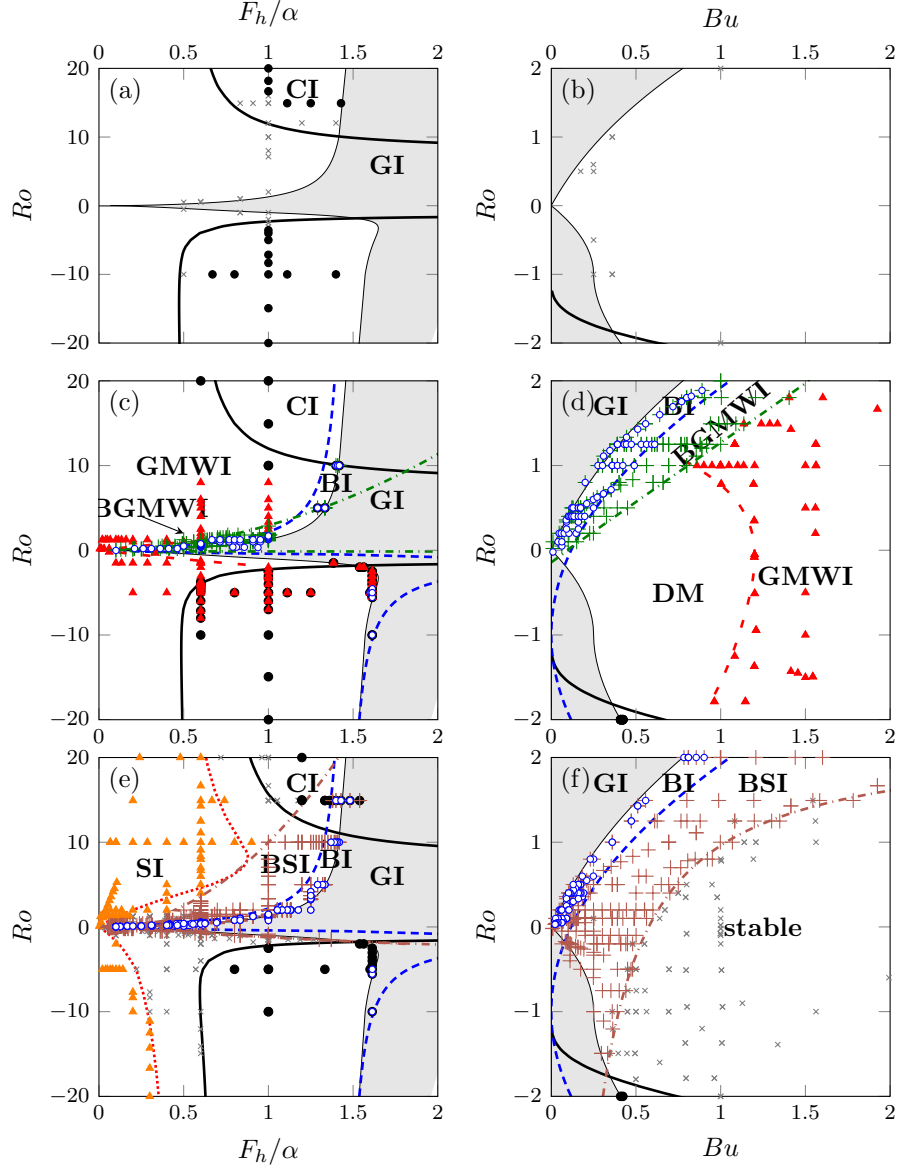


Figure 39: (Colour online) Domains of existence of the different instabilities for the azimuthal wavenumbers (a,b) $m = 0$, (c,d) $m = 1$ and (e,f) $m = 2$ as a function of Ro and F_h/α (a,c,e) and $Bu = Ro^2\alpha^2/(4F_h^2)$ (b,d,f) for $Re = 10000$ and various aspect ratio α . The symbols indicate the different instabilities for each set of parameters investigated: In (a-f): centrifugal (CI) \bullet ; baroclinic (BI) \circ ; and stable (\times). In (c,d): Gent-McWilliams (GMWI) \blacktriangle ; baroclinic-Gent-McWilliams (BGMWI) $+$. In (e,f): shear (SI) \blacktriangle and baroclinic-shear (BSI) $+$ instabilities. In the white region in (d), only the displacement mode (DM) is unstable for finite Re . The shaded area indicates the gravitationally unstable region (GI), the thick solid line shows the threshold for centrifugal instability for $\alpha = 0.5$ derived from (18), the dotted line is the threshold $F_h/\alpha < c(Ro)/\pi$ for shear instability and the dashed line is the threshold for baroclinic instability: $F_h/\alpha|1 + 1/Ro| = 1.46$. The dashed dotted lines in (c,d) and (e,f) show the empirical thresholds for baroclinic-Gent-McWilliams instability ($Bu = 0.7Ro + 0.1$) and baroclinic-shear instability ($Bu = 1.3/(-Ro + 2.26)$ for $|Ro| < 2$ and $Bu = 2.5Ro$ for $Ro > 2$) instabilities, respectively.

10 Conclusions

We have investigated the stability of an axisymmetric pancake vortex with Gaussian angular velocity in both radial and vertical directions in stratified rotating fluids. In stratified non-rotating fluids, Yim & Billant (2016) (part 1) have shown that such a pancake vortex can be unstable to centrifugal, shear, baroclinic and gravitational instabilities. Centrifugal instability occurs when the buoyancy Reynolds number $\mathcal{R} = ReF_h^2$ is sufficiently large regardless of the aspect ratio while the three other instabilities are mostly governed by the vertical Froude number F_h/α when the Reynolds number is large. Shear instability develops when $F_h/\alpha \leq 0.5$ whereas baroclinic and gravitational instabilities are active when $F_h/\alpha \geq 1.46$ and $F_h/\alpha \geq 1.5$, respectively. In contrast, in quasi-geostrophic fluids, Nguyen *et al.* (2012) found that, baroclinic instabilities are dominant for small Burger number $Bu = \alpha^2 Ro^2 / (4F_h^2) < 1$ while barotropic instabilities are dominant for $Bu > 1$.

In order to link the two limits: stratified non-rotating fluids and quasi-geostrophic fluids, we have first investigated the effects of the Rossby number for fixed aspect ratio α , Froude number F_h and Reynolds number Re . Then, the effects of the other parameters have been investigated for a fixed Rossby number. When $|Ro|$ is large, centrifugal instability is dominant since the generalized Rayleigh discriminant Φ is negative. As Ro decreases, it is stabilized before that Φ becomes positive everywhere because of viscous effects. The asymptotic formula for the growth rate of centrifugal instability for columnar vortices for large axial wavenumber (Billant & Gallaire, 2005), with the addition of leading viscous effects, works well also for pancake vortices for $m = 0$ and $m = 2$. For $m = 1$, it is in good agreement with the numerical results only for negative Rossby numbers. For moderate positive Rossby numbers, there is a discrepancy both for columnar and pancake vortices because centrifugal instability merges continuously with Gent-McWilliams instability. The latter instability is due to the presence of a critical radius where $\Omega = \omega_r$ in which the radial gradient of vertical vorticity is positive $\partial\zeta/\partial r > 0$ (Gent & McWilliams, 1986; Yim & Billant, 2015). Its growth rate for pancake vortices is mostly a function of F_h/α and Ro . The particular dependence with F_h/α has been explained qualitatively by considering the columnar configuration and confinement effects. Gent-McWilliams instability is the dominant instability for $m = 1$ in the centrifugally stable regime for $Bu \gtrsim 1$. For small Burger number $Bu \lesssim 0.7Ro + 0.1$, it transforms into a mixed baroclinic-Gent-McWilliams instability for which the energy source is no longer the kinetic energy but the potential energy of the base flow. Its growth rate is also mainly a function of F_h/α and Ro . Just below the threshold for the gravitational instability, baroclinic-Gent-McWilliams instability merges with the pure baroclinic instability. For $m = 1$, the displacement mode which derives from the translational invariance is also weakly unstable. It is destabilized by viscous effects since its growth rate is maximum for a finite Reynolds number and vanishes for $Re \rightarrow \infty$. It is the sole instability for $m = 1$ in an intermediate range of Burger number for $|Ro| < 2$.

Shear instability for $m = 2$ exists when $F_h/\alpha \leq c(Ro)/\pi$ where c is defined in (30). This condition derives directly from the fact that shear instability for a columnar vortex exists in the vertical wavenumber band $0 \leq kRF_h \leq c(Ro)$. The minimum wavenumber fitting inside the pancake vortex $kR = \pi/\alpha$, is therefore unstable only when $F_h/\alpha \leq c(Ro)/\pi$. In addition, the growth rate of shear

instability for pancake vortices depends also mostly on F_h/α and Ro and agrees well with the one of columnar vortices for the wavenumber $kR = \pi/\alpha$. When the Burger number is small ($Bu \lesssim 1.3/(-Ro + 2.26)$ for $|Ro| < 2$ and $Bu \lesssim 2.5Ro$ for $Ro > 2$), shear instability transforms into a mixed baroclinic-shear instability whose energy source is the potential energy of the base flow instead of the kinetic energy. Just below the threshold for the gravitational instability, the pure baroclinic instability is triggered and both baroclinic-shear and baroclinic instabilities can co-exist. Baroclinic instability can also destabilize higher wavenumbers $m \geq 3$.

An analytical model consisting in a bounded vortex with an angular velocity only varying slowly in the vertical direction has allowed us to show that the maximum growth rate and the most amplified azimuthal wavenumber of baroclinic instability should scale as $F_h/\alpha|1 + 1/Ro|$ in good agreement with the numerical results for positive Rossby numbers. Baroclinic instability develops only when $F_h/\alpha|1 + 1/Ro| \geq 1.46$. For negative Rossby numbers around $Ro = -1$, the model breaks down because the hypothesis of small vertical variation of the angular velocity compared to the absolute angular velocity $\Omega_0 + f/2$ no longer holds.

In this paper, we have considered a vortex which rotates in the same direction throughout the vertical. In the future, it could be interesting to study the stability of vortices whose angular velocity has not the same sign along the vertical as considered by Dewar & Killworth (1995); Killworth *et al.* (1997); Dewar *et al.* (1999) in two layer shallow-water rotating fluids and Nguyen *et al.* (2012) in continuously stratified quasi-geostrophic fluids. It would be also interesting to study the finite amplitude evolutions of the instabilities described herein.

We are very grateful to X. Garnaud for providing his numerical code and to D. Guy and V. D. Chi Toai for their technical assistances. This work was supported by the National Research Agency (ANR 2011 Blanc SIMI 5-6 012-02).

A Non-dimensionalization of the Euler equations for small Froude and Rossby numbers

In this appendix, we non-dimensionalize the equations (8)–(12) when the stratification is strong and the rotation is rapid. In addition, we show that the quasi-geostrophic approximation is obtained as long as Ro and F_h are small but the magnitude of the aspect ratio α can be arbitrary. This differs from the original derivation of the quasi-geostrophic equation by Charney & Stern (1962) where the main assumptions are $Ro \ll 1$, $\alpha \ll 1$ and $Bu = \alpha^2 Ro^2 / (4F_h^2) = O(1)$. A similar alternative derivation based on the smallness of the Froude number F_h is discussed in Vallis (2006). We define dimensionless quantities denoted by a hat for the base flow

$$\Omega = \Omega_0 \hat{\Omega}, \quad \zeta = \Omega_0 \hat{\zeta}, \quad p_t = \frac{\Omega_0 f R^2}{2} \hat{p}_t, \quad \rho_b = \frac{\rho_0 R \Omega_0 f}{2g\alpha} \hat{\rho}_b, \quad (40)$$

and for the perturbations

$$\begin{aligned} u_r = \Omega_0 R \hat{u}_r, \quad u_\theta = \Omega_0 R \hat{u}_\theta, \quad u_z = W \hat{u}_z, \quad p = \frac{\Omega_0 f R^2}{2} \hat{p}, \quad \rho = \frac{\Omega_0 f R}{2\alpha} \hat{\rho}, \\ r = R \hat{r}, \quad z = \Lambda \hat{z}, \quad \omega = \Omega_0 \hat{\omega}, \end{aligned} \quad (41)$$

where W is the unknown magnitude of the vertical velocity. The pressure and density scales have been chosen so that the geostrophic and hydrostatic balances hold for small Ro and F_h . For simplicity, we will consider an inviscid and non-diffusive fluid.

Inserting the scales (40)–(41) into (8)–(12) with $\nu = \kappa = 0$ give

$$Ro \left(-i(\hat{\omega} - m\hat{\Omega})\hat{u}_r - 2\hat{\Omega}\hat{u}_\theta \right) - 2\hat{u}_\theta = -\frac{\partial \hat{p}}{\partial \hat{r}}, \quad (42)$$

$$Ro \left(-i(\hat{\omega} - m\hat{\Omega})\hat{u}_\theta + \hat{\zeta}\hat{u}_r + \frac{W}{\Omega_0 R \alpha} \frac{\partial \hat{r}\hat{\Omega}}{\partial \hat{z}} \hat{u}_z \right) + 2\hat{u}_r = -\frac{im}{\hat{r}} \hat{p}, \quad (43)$$

$$-\frac{RoW\alpha}{\Omega_0 R} i(\hat{\omega} - m\hat{\Omega})\hat{u}_z = -\frac{\partial \hat{p}}{\partial \hat{z}} - \hat{\rho}, \quad (44)$$

$$-i(\hat{\omega} - m\hat{\Omega})\hat{\rho} + \frac{\partial \hat{\rho}_b}{\partial \hat{r}} \hat{u}_r + \frac{W}{\Omega_0 R \alpha} \frac{\partial \hat{\rho}_b}{\partial \hat{z}} \hat{u}_z = \frac{W\alpha Ro}{\Omega_0 R F_h^2} \hat{u}_z, \quad (45)$$

$$\frac{1}{\hat{r}} \frac{\partial \hat{r}\hat{u}_r}{\partial \hat{r}} + \frac{1}{\hat{r}} im\hat{u}_\theta + \frac{W}{\Omega_0 R \alpha} \frac{\partial \hat{u}_z}{\partial \hat{z}} = 0. \quad (46)$$

It is also useful to write the equation for the potential vorticity

$$i(-\hat{\omega} + m\hat{\Omega})\hat{\Pi} + \hat{u}_r \frac{\partial \hat{\Pi}_b}{\partial \hat{r}} + \hat{u}_z \frac{W}{\Omega_0 R \alpha} \frac{\partial \hat{\Pi}_b}{\partial \hat{z}} = 0, \quad (47)$$

where $\hat{\Pi}_b$ and $\hat{\Pi}$ are the non-dimensionalized potential vorticities of the base flow and the perturbation, respectively:

$$\hat{\Pi}_b = 1 + \frac{Ro}{2} \hat{\zeta} - \frac{F_h^2}{Ro\alpha^2} \frac{\partial \hat{\rho}_b}{\partial \hat{z}} - \frac{F_h^2}{2\alpha^2} \left(\hat{\zeta} \frac{\partial \hat{\rho}_b}{\partial \hat{z}} - \hat{r} \frac{\partial \hat{\Omega}}{\partial \hat{z}} \frac{\partial \hat{\rho}_b}{\partial \hat{r}} \right), \quad (48)$$

$$\hat{\Pi} = \frac{Ro}{2} \hat{w}_z - \frac{\partial \hat{\rho}}{\partial \hat{z}} \frac{F_h^2}{Ro\alpha^2} - \frac{F_h^2}{2\alpha^2} \left(\hat{w}_z \frac{\partial \hat{\rho}_b}{\partial \hat{z}} + \hat{w}_r \frac{\partial \hat{\rho}_b}{\partial \hat{r}} \right) - \frac{F_h^2}{2\alpha^2} \left(\hat{\zeta} \frac{\partial \hat{\rho}}{\partial \hat{z}} - \hat{r} \frac{\partial \hat{\Omega}}{\partial \hat{z}} \frac{\partial \hat{\rho}}{\partial \hat{r}} \right), \quad (49)$$

where \hat{w}_z and \hat{w}_r are the vertical and radial vorticity components of the perturbation. To be consistent, the equations (42)–(46) require that

$$W \leq \min \left(\Omega_0 R \alpha, \Omega_0 R \frac{F_h^2}{Ro\alpha} \right), \quad (50)$$

so that no term is larger than unity and so unbalanced. This implies that the order of magnitude of the vertical acceleration term in (44) is

$$\frac{\alpha W Ro}{\Omega_0 R} \leq \min (\alpha^2 Ro, F_h^2). \quad (51)$$

Therefore, whatever α and W , this term is at most $O(F_h^2)$ and thus very small when $F_h \ll 1$. Equations (42), (43) and (44) reduce therefore at leading order to the geostrophic and hydrostatic balances:

$$-2\hat{u}_\theta = -\frac{\partial \hat{p}}{\partial \hat{r}} + O(Ro), \quad (52)$$

$$2\hat{u}_r = -\frac{im}{\hat{r}} \hat{p} + O(Ro), \quad (53)$$

$$0 = -\frac{\partial \hat{p}}{\partial \hat{z}} - \hat{\rho} + O(F_h^2), \quad (54)$$

When $Ro \ll 1$, the terms $O(F_h^2/\alpha^2)$ in the potential vorticities (48)–(49) can be neglected compared to the terms $O(F_h^2/(Ro\alpha^2))$ regardless of the value of α . Hence, (48)–(49) reduce to

$$\hat{\Pi}_b = 1 + \frac{Ro}{2} \hat{\zeta} - \frac{F_h^2}{Ro\alpha^2} \frac{\partial \hat{\rho}_b}{\partial \hat{z}}, \quad (55)$$

$$\hat{\Pi} = \frac{Ro}{2} \hat{w}_z - \frac{\partial \hat{\rho}}{\partial \hat{z}} \frac{F_h^2}{Ro\alpha^2}. \quad (56)$$

We emphasize that the two last terms in (55) and (56) do not need to be of the same order for these equations to be valid, i.e. the Burger number is not needed to be of order unity. Indeed, (55) and (56) are the leading order expressions of the potential vorticity for $Ro \ll 1$ and $F_h \ll 1$ whatever the value of the Burger number. Using (52)–(54), the potential vorticity of the perturbation can be written

$$\hat{\Pi} = \frac{Ro}{4} \left[\frac{1}{\hat{r}} \frac{\partial}{\partial \hat{r}} \left(\hat{r} \frac{\partial \hat{p}}{\partial \hat{r}} \right) - \frac{m^2}{\hat{r}^2} \hat{p} \right] + \frac{F_h^2}{Ro\alpha^2} \frac{\partial^2 \hat{p}}{\partial \hat{z}^2}, \quad (57)$$

which is nothing than the quasi-geostrophic approximation of the potential vorticity of the perturbation. Using (2)–(3), the potential vorticity of the base flow reduces similarly to

$$\hat{\Pi}_b = 1 + \frac{Ro}{4} \frac{1}{\hat{r}} \frac{\partial}{\partial \hat{r}} \left(\hat{r} \frac{\partial \hat{p}_t}{\partial \hat{r}} \right) + \frac{F_h^2}{Ro\alpha^2} \frac{\partial^2 \hat{p}_t}{\partial \hat{z}^2}. \quad (58)$$

Furthermore, introducing (52)–(53) into (46) implies that $W/(\Omega_0 Ro) \leq Ro$ since the horizontal flow is nearly non-divergent. Thus, the vertical velocity in (47) can be neglected, giving the quasi-geostrophic equation for the potential vorticity

$$i(-\hat{\omega} + m\hat{\Omega})\hat{\Pi} + \hat{u}_r \frac{\partial \hat{\Pi}_b}{\partial \hat{r}} = 0. \quad (59)$$

We emphasize that the only assumptions used to derive (57)–(59) are $Ro \ll 1$ and $F_h \ll 1$ but the aspect ratio α has been considered arbitrary. In other words, the Burger number is not needed to be of order unity for the quasi-geostrophic approximation to hold in this derivation. However, it should be kept in mind that if the Burger number is very small, $Bu \leq Ro/4.5$, the base vortex is statically unstable (see (14)–(15)).

B Validation of the numerical code in the quasi-geostrophic limit for $Bu = 1$

In this appendix, we show that the quasi-geostrophic equation (59) can be solved by separation of variables for $Bu = 1$ when expressed in rescaled spherical coordinates. Hence, this particular case can be used as a validation test for the stability code based on FreeFEM++ and SLEPc. Equation (59) can be rewritten

$$(m\hat{\Omega} - \hat{\omega})\Delta \hat{p} - m \frac{\hat{p}}{\hat{r}} \frac{\partial \Delta \hat{p}_t}{\partial \hat{r}} = 0, \quad (60)$$

where $\Delta p = 1/\hat{r} \partial(\hat{r} \partial \hat{p}/\partial \hat{r})/\partial \hat{r} - m^2/\hat{r}^2 \hat{p} + 1/Bu \partial^2 \hat{p}/\partial \hat{z}^2$ and

	$m = 1$	$m = 1$	$m = 2$
Quasi-geostrophic limit, $Bu = 1$	0	0.0825-0.0030i	0.1650-0.0061i
$F_h = 0.05, Ro = 0.02, \alpha = 5, Re = 10000$	-0.00123+0.00061i	0.0846-0.0026i	0.1666-0.0059i
$F_h = 0.05, Ro = -0.02, \alpha = 5, Re = 10000$	-0.00128+0.00065i	0.0837-0.0026i	0.1658-0.0060i
$F_h = 0.01, Ro = 0.04, \alpha = 0.5, Re = 25000$	-0.00123+0.00052i	0.0837-0.0035i	0.1659-0.0067i
$F_h = 0.01, Ro = -0.04, \alpha = 0.5, Re = 25000$	-0.00121+0.00053i	0.0817-0.0036i	0.1641-0.0068i

Table 1: Comparison between the eigenvalues obtained by solving the quasi-geostrophic equation (60) for $Bu = 1$ with a shooting method and the stability code based on FreeFEM++ and SLEPc for small Froude and Rossby numbers approaching the quasi-geostrophic limit, large Reynolds number and aspect ratios such that $Bu = 1$.

$\Delta \hat{p}_t = 1/\hat{r} \partial(\hat{r} \partial \hat{p}_t / \partial \hat{r}) / \partial \hat{r} + 1/Bu \partial^2 \hat{p}_t / \partial \hat{z}^2$ with $\hat{p}_t = -\hat{\Omega}/4 = -e^{-\hat{r}^2 - \hat{z}^2}/4$ because of the non-dimensionalization (40)–(41).

When $Bu = 1$, (60) can be re-expressed as

$$\frac{1}{\xi^2} \frac{\partial}{\partial \xi} \left(\xi^2 \frac{\partial \hat{p}}{\partial \xi} \right) + \frac{1}{\xi^2 \sin \varphi} \frac{\partial}{\partial \varphi} \left(\sin \varphi \frac{\partial \hat{p}}{\partial \varphi} \right) - \frac{m^2 \hat{p}}{\xi^2 \sin^2 \varphi} - \frac{\hat{p}(-10 + 4\xi^2)e^{-\xi^2}}{e^{-\xi^2} - \hat{c}} = 0, \quad (61)$$

where (ξ, φ) are spherical coordinates such that $(\hat{r}, \hat{z}) = (\xi \sin \varphi, \xi \cos \varphi)$ and $\hat{c} = \hat{\omega}/m$. Then, (61) can be solved by separation of variables

$$\hat{p} = f(\xi)g(\varphi), \quad (62)$$

where $g(\phi)$ are associated Legendre functions

$$g(\varphi) = P_l^m(\cos \varphi) \quad (63)$$

with l an integer, while f satisfies

$$f'' + \frac{2f'}{\xi} - l(l+1)\frac{f}{\xi^2} - \frac{f(-10 + 4\xi^2)e^{-\xi^2}}{e^{-\xi^2} - \hat{c}} = 0 \quad (64)$$

The eigenvalue problem (64) has been solved by a shooting method with the boundary conditions $f(0) = 0$ and $f \rightarrow 0$ as $\xi \rightarrow \infty$. We found $\hat{c} \equiv \hat{c}_1 = 0$ for $l = 1$ and $\hat{c} \equiv \hat{c}_2 = 0.0825 - 0.0030i$ for $l = 2$. Thus, there is no instability for $Bu = 1$ in the quasi-geostrophic and inviscid limits. Since associated Legendre functions exist only for $m \leq l$, this corresponds to two eigenvalues for $m = 1$, $\hat{\omega} = \hat{c}_1$ (which corresponds to the neutral displacement mode) and $\hat{\omega} = \hat{c}_2$ and one eigenvalue for $m = 2$, $\hat{\omega} = 2\hat{c}_2$. These eigenvalues for $m = 1$ and $m = 2$ are compared in table 1 to those obtained with the full stability code for small Rossby and Froude numbers approaching the quasi-geostrophic limit and two distinct aspect ratios $\alpha = 5$ and $\alpha = 0.5$ such that $Bu = 1$. For $F_h = 0.01$, the Reynolds number has been increased to $Re = 25000$ in order to have the same buoyancy Reynolds number as for $F_h = 0.05$ and $Re = 10000$. A good agreement between the two numerical methods is found for each case. The discrepancies are of the same order as the differences between the eigenvalues for the two Froude numbers investigated. Hence, it is expected that these discrepancies would decrease for smaller Ro and F_h provided that the buoyancy Reynolds number ReF_h^2 is sufficiently high.

References

- ABRAMOWITZ, M. & STEGUN, I. A. 1972 *Handbook of Mathematical Functions*. New York: Dover.
- ANTKOWIAK, A. & BRANCHER, P. 2004 Transient energy growth for the lamb-oseen vortex. *Phys. Fluids* **16**, L1–L4.
- ARMI, L., HEBERT, D., OAKEY, N., PRICE, J. F., RICHARDSON, P. L., ROSSBY, H. T. & RUDDICK, B. 1989 Two years in the life of a mediterranean salt lens. *J. Phys. Oceanogr.* **19**, 354370.
- AUBERT, O., LE BARS, M., LE GAL, P. & MARCUS, P. S. 2012 The universal aspect ratio of vortices in rotating stratified flows: experiments and observations. *J. Fluid Mech.* **706**, 34–45.
- BAEY, J.-M. & CARTON, X. 2002 Vortex multipoles in two-layer rotating shallow-water flows. *J. Fluid Mech.* **460**, 151–175.
- BALAY, S., ABHYANKAR, S., ADAMS, M. F., BROWN, J., BRUNE, P., BUSCHELMAN, K., ELJKHOUT, V., GROPP, W. D., KAUSHIK, D., KNEPLEY, M. G., MCINNES, L. C., RUPP, K., SMITH, B. F. & ZHANG, H. 2014 PETSc users manual. *Tech. Rep.* ANL-95/11 - Revision 3.5. Argonne National Laboratory.
- BENILOV, E. 2003 Instability of quasi-geostrophic vortices in a two-layer ocean with a thin upper layer. *J. Fluid Mech.* **475**, 303–331.
- BILLANT, P. 2010 Zigzag instability of vortex pairs in stratified and rotating fluids. part 1. general stability equations. *J. Fluid Mech.* **660**, 354–395.
- BILLANT, P., COLETTE, A. & CHOMAZ, J.-M. 2004 Instabilities of a vortex pair in a stratified and rotating fluid. *Proceedings of the 21st International Congress of the International Union of Theoretical and Applied Mechanics, Varsovie* pp. 16–20.
- BILLANT, P. & GALLAIRE, F. 2005 Generalized rayleigh criterion for non-axisymmetric centrifugal instabilities. *J. Fluid Mech.* **542**, 365–379.
- BLUMEN, W. 1971 On the stability of a barotropic shear flow to nongeostrophic disturbances. *Tellus* **23** (4-5), 295–301.
- CARTON, X. 2001 Hydrodynamical modeling of oceanic vortices. *Surv. Geophys.* **22** (3), 179–263.
- CARTON, X., LE CANN, B., SERPETTE, A. & DUBERT, J. 2013 Interactions of surface and deep anticyclonic eddies in the bay of biscay. *J. Marine Syst.* **109–110**, S45 – S59, xII International Symposium on Oceanography of the Bay of Biscay.
- CHANG, K.-I., TEAGUE, W. J., LYU, S. J., PERKINS, H. T., LEE, D.-K., WATTS, D. R., Y.-B., KIM., MITCHELL, D. A., LEE, C. M. & KIM, K. 2004 Circulation and currents in the southwestern east/japan sea: Overview and review. *Prog. Oceanogr.* **61** (24), 105 – 156.

- CHARNEY, J. G. & STERN, M. E. 1962 On the stability of internal baroclinic jets in a rotating atmosphere. *J. Atmos. Sci.* **19** (2), 159–172.
- DEWAR, W. K. & KILLWORTH, P. D. 1995 On the stability of oceanic rings. *J. Phys. Oceanogr.* **25**, 1467–1487.
- DEWAR, W. K., KILLWORTH, P. D. & BLUNDELL, J. R. 1999 Primitive-equation instability of wide oceanic rings. part ii: numerical studies of ring stability. *J. Phys. Oceanogr.* **29**, 1744–1758.
- DRAZIN, P.G. & REID, W.H. 1981 *Hydrodynamic Stability. Cambridge Mathematical Library* 1. Cambridge University Press.
- DRITSCHEL, D. G. & MCKIVER, W. J. 2015 Effect of prandtl's ratio on balance in geophysical turbulence. *J. Fluid Mech.* **777**, 569–590.
- DRITSCHEL, D. G., DE LA TORRE JUÁREZ, M. & AMBAUM, M. H. P. 1999 The three-dimensional vortical nature of atmospheric and oceanic turbulent flows. *Phys. Fluids* **11** (6), 1512–1520.
- EADY, E. T. 1949 Long waves and cyclone waves. *Tellus* **1** (3), 33–52.
- ELIASSEN, A. 1983 The charney-stern theorem on barotropic-baroclinic instability. *Pure Appl. Geophys.* **121** (3), 563–572.
- ELIASSEN, A. & KLEINSCHMIDT, E. JR. 1957 Dynamic meteorology. In *Geophysik II / Geophysics II* (ed. Julius Bartels), *Handbuch der Physik / Encyclopedia of Physics*, vol. 10 / 48, pp. 1–154. Springer Berlin Heidelberg.
- FLIERL, G. R. 1988 On the instability of geostrophic vortices. *J. Fluid Mech.* **197**, 349–388.
- FORD, R. 1994 The instability of an axisymmetric vortex with monotonic potential vorticity in rotating shallow water. *J. Fluid Mech.* **280**, 303–334.
- GARNAUD, X. 2012 Modes, transient dynamics and forced response of circular jets. PhD thesis, LadHyX, Ecole Polytechnique X.
- GARNAUD, X., LESSHAFFT, L., SCHMID, P. J. & HUERRE, P. 2013 Modal and transient dynamics of jet flows. *Phys. Fluids* **25** (4).
- GENT, P. R. & MCWILLIAMS, J. C. 1986 The instability of barotropic circular vortices. *Geophys. Astrophys. Fluid Dyn.* **35** (1-4), 209–233.
- GILL, A. E. 1981 Homogeneous intrusions in a rotating stratified fluid. *J. Fluid Mech.* **103**, 275–295.
- GRIFFITHS, R. W. & LINDEN, P. F. 1981 The stability of vortices in a rotating, stratified fluid. *J. Fluid Mech.* **105**, 283–316.
- HASSANZADEH, P., MARCUS, P. S. & LE GAL, P. 2012 The universal aspect ratio of vortices in rotating stratified flows: theory and simulation. *J. Fluid Mech.* **706**, 46–57.
- HECHT, F. 2012 New development in freefem++. *J. Numer. Math.* **20** (3-4), 251–265.

- HEDSTROM, K. & ARMI, L. 1988 An experimental study of homogeneous lenses in a stratified rotating fluid. *J. Fluid Mech.* **191**, 535–556.
- HELFRICH, K. R. & SEND, U. 1988 Finite-amplitude evolution of two-layer geostrophic vortices. *J. Fluid Mech.* **197**, 331–348.
- HERNANDEZ, V., ROMAN, J. E. & VIDAL, V. 2005 SLEPc: A scalable and flexible toolkit for the solution of eigenvalue problems. *ACM Trans. Math. Software* **31** (3), 351–362.
- HIDE, R. & MASON, P. J. 1975 Sloping convection in a rotating fluid. *Adv. Phys.* **24** (1), 47–100.
- HOBBS, R. 2007 Go (geophysical oceanography): a new tool to understand the thermal structure and dynamics of oceans. *European Union Newsletter* **2**.
- HOPFINGER, E. J. & VAN HEIJST, G. J. F. 1993 Vortices in rotating fluids. *Annu. Rev. Fluid Mech.* **25** (1), 241–289.
- HOSKINS, B. J., MCINTYRE, M. E. & ROBERTSON, A. W. 1985 On the use and significance of isentropic potential vorticity maps. *Quart. J. R. Met. Soc.* **111** (470), 877–946.
- HUA, B. L., MÉNESGUEN, C., LE GENTIL, S., SCHOPP, R., MARSET, B. & AIKI, H. 2013 Layering and turbulence surrounding an anticyclonic oceanic vortex: in situ observations and quasi-geostrophic numerical simulations. *J. Fluid Mech.* **731**, 418–442.
- IKEDA, M. 1981 Instability and splitting of mesoscale rings using a two-layer quasi-geostrophic model on an f -plane. *J. Phys. Oceanogr.* **11** (7), 987–998.
- KILLWORTH, P. D., BLUNDELL, J. R. & DEWAR, W. K. 1997 Primitive equation instability of wide oceanic rings. part i: linear theory. *J. Phys. Oceanogr.* **27**, 941–962.
- KIM, D., YANG, E., KIM, K., SHIN, C., PARK, J., YOO, S. & HYUN, J. 2012 Impact of an anticyclonic eddy on the summer nutrient and chlorophyll a distributions in the ulleung basin, east sea (japan sea). *J. Marine Syst.* **69** (1), 23–29.
- LAHAYE, N. & ZEITLIN, V. 2015 Centrifugal, barotropic and baroclinic instabilities of isolated ageostrophic anticyclones in the two-layer rotating shallow water model and their nonlinear saturation. *J. Fluid Mech.* **762**, 5–34.
- LAZAR, A., STEGNER, A., CALDEIRA, R., DONG, C., DIDELLE, H. & VIBOUD, S. 2013*a* Inertial instability of intense stratified anticyclones. part 2. laboratory experiments. *J. Fluid Mech.* **732**, 485–509.
- LAZAR, A., STEGNER, A. & HEIFETZ, E. 2013*b* Inertial instability of intense stratified anticyclones. part 1. generalized stability criterion. *J. Fluid Mech.* **732**, 457–484.
- MCINTYRE, M. E. 1970 Diffusive destabilization of the baroclinic circular vortex. *Geophys. Fluid Dyn.* **1**, 19–57.

- MÉNESGUEN, C., HUA, B. L., CARTON, X., KLINGELHOEFER, F., SCHNRLÉ, P. & REICHERT, C. 2012*a* Arms winding around a meddy seen in seismic reflection data close to the morocco coastline. *Geophys. Res. Lett.* **39** (5), L05604.
- MÉNESGUEN, C., MCWILLIAMS, J. C. & MOLEMAKER, M. J. 2012*b* Ageostrophic instability in a rotating stratified interior jet. *J. Fluid Mech.* **711**, 599–619.
- MESCHANOV, S.L. & SHAPIRO, G.I. 1998 A young lens of red sea water in the arabian sea. *Deep-Sea Res. Pt. I* **45** (1), 1 – 13.
- NEGRETTE, M. E. & BILLANT, P. 2013 Stability of a gaussian pancake vortex in a stratified fluid. *J. Fluid Mech.* **718**, 457–480.
- NGUYEN, H. Y., HUA, B. L., SCHOPP, R. & CARTON, X. 2012 Slow quasi-geostrophic unstable modes of a lens vortex in a continuously stratified flow. *Geophys. Astrophys. Fluid Dyn.* **106** (3), 305–319.
- PINGREE, R. D. & LE CANN, B. 1992 Anticyclonic eddy x91 in the southern bay of biscay, may 1991 to february 1992. *J. Geophys. Res.* **97** (C9), 14353–14367.
- REINAUD, J. N., DRITSCHER, D. G. & KOUDELLA, C. R. 2003 The shape of vortices in quasi-geostrophic turbulence. *J. Fluid Mech.* **474**, 175–192.
- RICHARDSON, P. L., BOWER, A. S. & ZENK, W. 2000 A census of meddies tracked by floats. *Prog. Oceanogr.* **45**, 209–250.
- RIEDINGER, X., LE DIZÈS, S. & MEUNIER, P. 2010 Viscous stability properties of a lamb-oseen vortex in a stratified fluid. *J. Fluid Mech.* **645**, 255–278.
- RIPA, P. 1991 General stability conditions for a multi-layer model. *J. Fluid Mech.* **222**, 119–137.
- ROMAN, J.E., CAMPOS, C., ROMERO, E. & TOMAS, A. 2015 SLEPc users manual. *Tech. Rep.* DSIC-II/24/02 - Revision 3.6. D. Sistemes Informàtics i Computació, Universitat Politècnica de València.
- SAUNDERS, P. M. 1973 The instability of a baroclinic vortex. *J. Phys. Oceanogr.* **3**, 61–65.
- SMYTH, W. D. & MCWILLIAMS, J. C. 1998 Instability of an axisymmetric vortex in a stably stratified, rotating environment. *Theor. Comp. Fluid Dyn.* **11** (3-4), 305–322.
- SOLBERG, H. 1936 Le mouvement d’inertie de l’atmosphère stable et son rôle dans la théorie des cyclones. In *Meteor. Assoc. U.G.G.I.*, pp. 66 – 82. Dupont.
- STEGNER, A. & DRITSCHER, D.G. 2000 A numerical investigation of the stability of isolated shallow water vortices. *J. Phys. Oceanogr.* **30**, 2562–2573.
- THIVOLLE-CAZAT, J., SOMMERIA, J. & GALMICHE, M. 2005 Baroclinic instability of two-layer vortices in laboratory experiments. *J. Fluid Mech.* **544**, 69–97.

- VALLIS, G.K. 2006 *Atmospheric and Oceanic Fluid Dynamics: Fundamentals and Large-scale Circulation*. Cambridge University Press.
- VERZICCO, R., LALLI, F. & CAMPANA, E. 1997 Dynamics of baroclinic vortices in a rotating, stratified fluid: A numerical study. *Phys. Fluids* **9** (2), 419–432.
- YIM, E. & BILLANT, P. 2015 On the mechanism of the gent-mcwilliams instability of a columnar vortex in stratified rotating fluids. *J. Fluid Mech.* **780**, 5–44.
- YIM, E. & BILLANT, P. 2016 Analogies and differences between the stability of an isolated pancake vortex and a columnar vortex in stratified fluid. *J. Fluid Mech.* **796**, 732–766.